DTU Physics
Department of Physics

Bachelor thesis

Theory and simulation of thermo-viscous ultrasound handling of microparticles and fluids

Gustav K. Modler
s173728

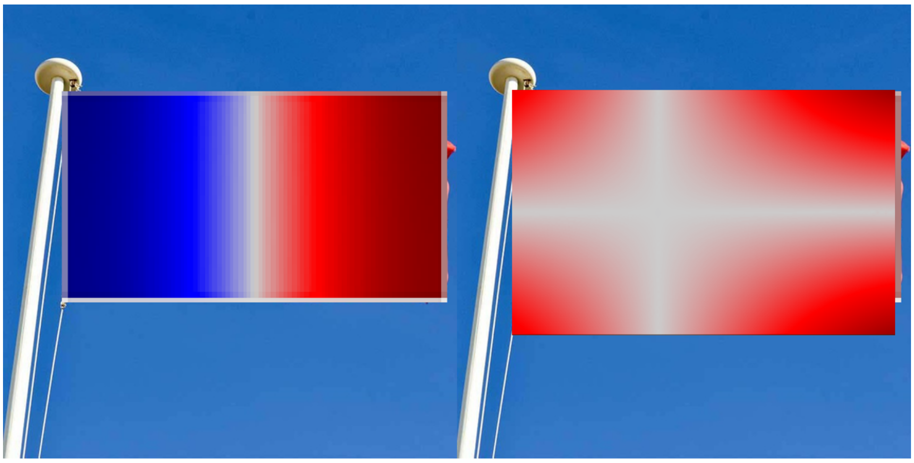

Supervisors: Henrik Bruus and Jonas Helboe Jørgensen

Department of Physics
Technical University of Denmark

14 June 2021

Abstract

This is a numerical study of an acoustofluidic device with an imposed temperature gradient in the horizontal direction. The device simply consists of a water-filled microchannel embedded in an elastic solid, which is actuated in the MHz-range to induce standing acoustic waves inside the channel.

The imposed temperature gradient induced gradients in the density and compressibility of the fluid, which gave rise to an acoustic body force in the bulk in the direction of the high temperature region. This force changed the acoustic streaming for the vertical half-wavelength mode, while hardly affecting those of the horizontal modes—although, for these two, the streaming did increase in the high temperature region and decrease in the low temperature one slightly. The streaming for the vertical mode transitioned from the characteristic four stream rolls along the sides of the channel to a horizontal streaming via the anti-nodes toward the high temperature region and a streaming via the node back to the low temperature region. The streaming via the anti-nodes was driven by the body force, but the streaming via the node occurred due to mass conservation. The body force was strongest in the anti-nodes because the compressibility of water is more temperature sensitive than its density.

Finally, the prospect of using this streaming to separate particles in the horizontal direction based on their acoustic contrast factor was discussed. At best, it could improve the succes rate at separating particles of different contrast factors by also separating them in the horizontal direction.

Resumé

I dette bachelorprojekt studeres en akustofluidisk mikrochip med en påtrykt temperaturgradient i den horisontale retning i simuleringsværtøjet COMSOL Multiphysics 5.6. Mikrochippen består af en vandkanal, der er omsluttet af et elastisk materiale, der aktueres i MHz-området, så stående akustiske bølger fremkommer i kanalen.

Den påtrykte temperaturgradient fremkaldte gradienter i vandets massefylde og kompressibilitet, hvormed en akustisk kraft i retningen af den høje temperatur fremkom. Denne kraft ændrede den akustiske strømning for den vertikale halvbølge-egentilstand, mens strømningerne for de horisontale egentilstande var hovedsagligt uberørte. Strømningen for den vertikale egentilstand ændrede sig fra de karakteristiske fire ruller langs siderne på kanalen til to horisontale strømninger via bølgetoppene i retningen af den høje temperatur, hvorefter de vendte tilbage via knudepunktet i retningen af den lave temperatur. Kraften var stærkest i bølgetoppene, for kompressibiliteten af væsken var mere følsom overfor temperaturændringer end dens massefylde.

Til sidst blev strømningen kort diskuteret i kontekst af at anvende den til mikropartikeladskillelse baseret på deres kontrast faktor. Strømningen kan adskille partiklerne i den horisontale retning, hvilket potentielt kan forbedre allerede etableret metoder for adskillelse af mikropartikler.

Preface

This work is submitted for the Bachelor of Science in Engineering degree (physics and nanotechnology) at the Technical University of Denmark, DTU. It was carried out at the Department of Physics in the Theoretical Microfluidics Group, headed by Prof. Henrik Bruus, from March, 2021 to June, 2021 with an accredited workload of 15 ECTS.

I want to thank my supervisors Prof. Henrik Bruus and PhD-student Jonas Helboe Jørgensen. They have been inspirational, encouraging, supportive and all around great supervisors, and I have learned a lot from them. Also, Prof. Bruus was readily available to speak about the project, even outside the scheduled meetings, for which I am very thankful.

Gustav Kildevang Modler
Department of Physics
Technical University of Denmark
14 June 2021

Contents

List of Figures

List of Tables

Chapter 1

Introduction

Acoustofluidic technology uses standing ultrasonic waves to manipulate particles and fluids on a sub-millimeter scale in lab-on-a-chip systems [1]. The acoustic waves are typically generated by the vibrations of an elastic solid, which is actuated in the MHz-range by a piezo-electric transducer [2]. The technology is regularly applied within cell biology and medicine for handling, sorting, mixing, and trapping of cells and bio-molecules [2–6].

Recent research has demonstrated the importance of thermoviscous effects in acoustofluidic microsystems. Notably, the thermoviscous treatment of the acoustic radiation force by Karlsen and Bruus [7] predicts forces which are several orders of magnitude larger than those of the ideal-fluid theory. Additionally, the effective thermoviscous model by Jørgensen and Bruus [8] shows that an in-homogeneous stationary temperature field influences the acoustic streaming by inducing a body force density in the bulk. The force is also supported by experimental evidence [9].

Inspired by Jørgensen and Bruus, this thesis is a numerical study of the effects of an imposed horizontal temperature gradient across an acoustofluidic device. The device consists of a water-filled microchannel enclosed by silicon on its sides and pyrex glass on its top and bottom. The superior thermal conductivity of silicon compared to water confines the temperature gradient to the microchannel. On the basis of a thermoviscous model by Muller and Bruus [10], both the microchannel and surrounding solids are modelled, but the transducer is represented by an imposed displacement field on parts of the outer boundaries of the solid.

Chapter 2

Theory

This chapter aims to provide the reader with the minimum knowledge of thermoviscous acoustofluidics required to follow this thesis. First, it introduces the governing equations of fluid dynamics, thermodynamics and heat transfer, and elastodynamics in Sections 2.1, 2.2, and 2.3. Then a thermoviscous acoustofluidic model, which was formulated by Muller and Bruus [10], is presented in Section 2.4. The field of acoustofluidics has progressed far since the conception of this model with the formulation of the viscous boundary layer theory by Bach and Bruus [11] as well as the thermoviscous boundary layer theory by Jørgensen and Bruus [8]. In spite of this, I use a full-scale model which can be run on my computer because I work in 2D and not 3D. Finally, in Section 2.5, the acoustic wave equation is derived.

2.1 Fluid dynamics

The governing equations of fluid dynamics are the continuity and the Navier–Stokes equations. They express the conservation of mass and momentum of an arbitrarily shaped body Ω of fluid, respectively. In terms of the mass-density field $\rho(\boldsymbol{r}, t)$ of the fluid, the local center-of-mass velocity field $\boldsymbol{v}(\boldsymbol{r}, t)$, and the stress-tensor field $\boldsymbol{\sigma}(\boldsymbol{r}, t)$, the equations are given by [12, 13]

$$\partial_t \rho = -\boldsymbol{\nabla} \cdot (\rho \boldsymbol{v}) \,, \tag{2.1a}$$

$$\partial_t (\rho \boldsymbol{v}) = \boldsymbol{\nabla} \cdot (\boldsymbol{\sigma} - \rho \boldsymbol{v}\boldsymbol{v}) \,. \tag{2.1b}$$

The continuity equation (2.1a) reads that any change in the total mass inside Ω is related to a mass-flux through the surface $\partial\Omega$ of the body by the mass current $\rho\boldsymbol{v}$. Likewise, from Eq. (2.1b), a change in the total momentum inside Ω is related to a momentum-flux through $\partial\Omega$ by the current $\rho\boldsymbol{v}\boldsymbol{v}$ or to stresses $\boldsymbol{\sigma}$ acting on $\partial\Omega$ [13, 14].

By convention, the fluid stress-tensor is resolved into a pressure term and a viscous term $\boldsymbol{\tau}$ [13],

$$\boldsymbol{\sigma} = -p\mathbf{1} + \boldsymbol{\tau} \,, \quad \boldsymbol{\tau} = \eta\big[\boldsymbol{\nabla}\boldsymbol{v} + (\boldsymbol{\nabla}\boldsymbol{v})^{\dagger}\big] + \big(\eta^{\mathrm{b}} - \tfrac{2}{3}\eta\big)(\boldsymbol{\nabla}\cdot\boldsymbol{v})\mathbf{1} \,. \tag{2.2}$$

Here η and η^{b} are the shear and bulk viscosities, respectively, and $\mathbf{1}$ is the unit tensor.

A viscous fluid does not slip along solid materials, and so we apply the standard no-slip condition at every fluid-solid boundary [12] (where the brackets denote the difference between the two sides of a boundary),

$$[\boldsymbol{v}] = \mathbf{0}\,, \qquad \text{at the fluid-solid boundaries.} \tag{2.3}$$

2.2 Thermodynamics

All material parameters of a thermoviscous fluid depend on the temperature T and the density ρ of the fluid. Representing any such parameter by q, this may be written as [8, 10]

$$\mathrm{d}q = \left(\frac{\partial q}{\partial T}\right)_\rho \mathrm{d}T + \left(\frac{\partial q}{\partial \rho}\right)_T \mathrm{d}\rho\,. \tag{2.4}$$

The temperature field $T(\boldsymbol{r}, t)$ couples to the other fields via the equation for conservation of energy [7, 8, 10, 15],

$$\partial_t\left(\rho\varepsilon + \frac{1}{2}\rho v^2\right) - P = \boldsymbol{\nabla}\cdot\left[\boldsymbol{v}\cdot\boldsymbol{\sigma} + k^{\mathrm{th}}\boldsymbol{\nabla}T - \rho\left(\varepsilon + \frac{1}{2}v^2\right)\boldsymbol{v}\right]\,. \tag{2.5}$$

Here ε is the specific internal energy, k^{th} the thermal conductivity, and P the power density from local heat sources and sinks.

The internal energy is related to the temperature and pressure by [10]

$$\rho\mathrm{d}\varepsilon = (\rho c_p - \alpha_p p)\,\mathrm{d}T - (\kappa_T p + \alpha_p T)\,\mathrm{d}p\,, \tag{2.6}$$

where c_p is the specific isobaric heat capacity, α_p the thermal expansivity, and κ_T the isothermal compressibility. The isentropic compressibility κ_s is related to κ_T by [10, 16]

$$\gamma\kappa_s = \kappa_T\,, \tag{2.7}$$

where γ is the ratio of heat capacities c_p and c_V,

$$\gamma \equiv \frac{c_p}{c_V} = 1 + \frac{T\alpha_p^2}{\rho c_V \kappa_s}\,, \tag{2.8}$$

which, for solids, equals unity within a few percent.

Finally, everything is reconciled to the temperature and pressure by the following equation of state [8, 10, 12]:

$$\frac{\mathrm{d}\rho}{\rho} = \kappa_T\mathrm{d}p - \alpha_p\mathrm{d}T\,. \tag{2.9}$$

2.3 Elastodynamics

The deformation of a solid body subjected to stresses acting on its surface is governed by Newton's second law. The state of deformation is described by the displacement field

$\boldsymbol{u}(\boldsymbol{r},t) = \boldsymbol{r}'(t) - \boldsymbol{r}(t)$ where $\boldsymbol{r}'$ is the position of point $\boldsymbol{r}$ after the deformation. In terms of this, the mass-density field $\rho(\boldsymbol{r},t)$ of the solid, and the solid stress-tensor field $\boldsymbol{\sigma}(\boldsymbol{r},t)$, Newton's second law takes the form [12, 14, 17]

$$\rho\partial_t^2\boldsymbol{u} = \boldsymbol{\nabla}\cdot\boldsymbol{\sigma}\,, \tag{2.10a}$$

where the anisotropic solid stress-tensor is given by

$$\boldsymbol{\sigma} = \rho c_{\mathrm{T}}^2\big[\boldsymbol{\nabla}\boldsymbol{u} + (\boldsymbol{\nabla}\boldsymbol{u})^\dagger\big] + \rho\big(c_{\mathrm{L}}^2 - 2c_{\mathrm{T}}^2\big)(\boldsymbol{\nabla}\cdot\boldsymbol{u})\mathbf{1}\,. \tag{2.10b}$$

In absence of body forces, the solutions take the form of waves which may be resolved into two components: a curl-less longitudinal component $\boldsymbol{u}_{\mathrm{L}}$ and a divergence-free transverse component $\boldsymbol{u}_{\mathrm{T}}$. Hence, the parameters c_{L} and c_{T} are the longitudinal and transverse speeds of propagation of said waves through the body, respectively. [12]

The boundary conditions express continuity of the displacement field and the stress-vector across material interfaces [12],

$$[\boldsymbol{u}] = \mathbf{0}\,, \tag{2.11a}$$

$$[\boldsymbol{\sigma}\cdot\hat{\boldsymbol{n}}] = \mathbf{0}\,. \tag{2.11b}$$

Here Eq. (2.11b) is a consequence of Newton's third law.

2.4 A thermoviscous acoustofluidic model

The system under consideration is a liquid-filled microchannel embedded in an elastic solid. The solid is actuated at a frequency f in the MHz range by a piezo-electric transducer, which induces standing acoustic waves inside the channel. The transducer is represented by an imposed displacement field $\boldsymbol{d}_0$ on parts of the outer boundary.

The model by Muller and Bruus [10] is formulated within the framework of perturbation theory. Perturbation theory aims to find an approximate solution to a complex problem by representing the solution as a power series in some small parameter $\epsilon \ll 1$. In acoustofluidics, this small parameter is $\frac{Qd_0\omega}{c}$, where Q is the Q-factor at resonance, d_0 the actuation displacement amplitude, and $\omega = 2\pi f$ the angular frequency.

To zeroth order, the system is at rest. Then, assuming time-harmonic first-order fields with angular frequency ω arising from the actuation, the fields to second order take the following form:

$$\mathcal{Q}(\boldsymbol{r},t) = \mathcal{Q}_0(\boldsymbol{r}) + \mathcal{Q}_1(\boldsymbol{r})\mathrm{e}^{-\mathrm{i}\omega t} + \mathcal{Q}_2(\boldsymbol{r},t)\,, \tag{2.12}$$

with $\boldsymbol{v}_0 = \mathbf{0}$ and $\boldsymbol{u}_0 = \mathbf{0}$. For the expansion (2.12) to be valid, we will need to verify that $\mathcal{Q}_2 \ll \mathcal{Q}_1 \ll \mathcal{Q}_0$ at the end of computations. Additionally, material parameters are written as

$$q(\boldsymbol{r},t) = q_0(T_0) + q_1(T_1,\rho_1)\mathrm{e}^{-\mathrm{i}\omega t}\,, \tag{2.13a}$$

$$q_1(T_1,\rho_1) = \left(\frac{\partial q}{\partial T}\right)_{\rho_0} T_1 + \left(\frac{\partial q}{\partial \rho}\right)_{T_0} \rho_1\,. \tag{2.13b}$$

On substituting Eqs. (2.12) and (2.13) into the governing equations (2.1), (2.5), and (2.10) and only keeping the first-order terms, the first-order equations become

$$\begin{aligned}
\rho_0 c_p \partial_t T_1 - \alpha_p T_0 \partial_t p_1 &= \boldsymbol{\nabla}\cdot\big(k_0^{\mathrm{th}}\boldsymbol{\nabla} T_1\big)\,, && (2.14\mathrm{a})\\
\rho_0(\kappa_T \partial_t p_1 - \alpha_p \partial_t T_1) &= -\boldsymbol{\nabla}\cdot(\rho_0 \boldsymbol{v}_1)\,, && (2.14\mathrm{b})\\
\rho_0 \partial_t \boldsymbol{v}_1 &= \boldsymbol{\nabla}\cdot(\boldsymbol{\tau}_1 - p_1\mathbf{1})\,, && (2.14\mathrm{c})\\
-\rho^{\mathrm{sl}}\omega^2(1+\mathrm{i}\Gamma^{\mathrm{sl}})^2\boldsymbol{u}_1 &= \boldsymbol{\nabla}\cdot\boldsymbol{\sigma}_1\,, && (2.14\mathrm{d})
\end{aligned}$$

where $\boldsymbol{\tau}_1$ and $\boldsymbol{\sigma}_1$ are

$$\begin{aligned}
\boldsymbol{\tau}_1 &= \eta_0\big[\boldsymbol{\nabla}\boldsymbol{v}_1 + (\boldsymbol{\nabla}\boldsymbol{v}_1)^\dagger\big] + \big(\eta_0^{\mathrm{b}} - \tfrac{2}{3}\eta_0\big)(\boldsymbol{\nabla}\cdot\boldsymbol{v}_1)\mathbf{1}\,, && (2.15\mathrm{a})\\
\boldsymbol{\sigma}_1 &= \rho^{\mathrm{sl}} c_{\mathrm{T}}^2\big[\boldsymbol{\nabla}\boldsymbol{u}_1 + (\boldsymbol{\nabla}\boldsymbol{u}_1)^\dagger\big] + \rho^{\mathrm{sl}}\big(c_{\mathrm{L}}^2 - 2c_{\mathrm{T}}^2\big)(\boldsymbol{\nabla}\cdot\boldsymbol{u}_1)\mathbf{1}\,. && (2.15\mathrm{b})
\end{aligned}$$

The boundary conditions (2.3) and (2.11) become

$$\begin{aligned}
\boldsymbol{v}_1 &= -\mathrm{i}\omega(1+\mathrm{i}\Gamma^{\mathrm{sl}})\boldsymbol{u}_1\,, && \text{at the fluid-solid boundaries;} && (2.16\mathrm{a})\\
\boldsymbol{u}_1 &= \boldsymbol{d}_0\,, && \text{at the place of actuation;} && (2.16\mathrm{b})\\
\boldsymbol{\sigma}_1\cdot\hat{\boldsymbol{n}} &= (\boldsymbol{\tau}_1 - p_1\mathbf{1})\cdot\hat{\boldsymbol{n}}\,, && \text{at the fluid-solid boundaries.} && (2.16\mathrm{c})
\end{aligned}$$

Proceeding to second order, all second-order fields and products of two first-order fields are time-averaged over an oscillation period, $\tau_{\mathrm{osc}} = \frac{2\pi}{\omega}$. This is denoted by angled brackets, but the notation gets suppressed on the second-order fields for the sake of brevity. The equations for the fields T_2 and $\boldsymbol{u}_2$ get omitted because the two fields do not enter the second-order continuity and Navier–Stokes equations. The second-order equations are thus

$$\begin{aligned}
0 &= \boldsymbol{\nabla}\cdot\big[\rho_0\boldsymbol{v}_2 + \langle\rho_1\boldsymbol{v}_1\rangle\big]\,, && (2.17\mathrm{a})\\
\mathbf{0} &= \boldsymbol{\nabla}\cdot\big[\boldsymbol{\tau}_2 - p_2\mathbf{1} - \rho_0\langle\boldsymbol{v}_1\boldsymbol{v}_1\rangle + \boldsymbol{\tau}_{11}\big]\,. && (2.17\mathrm{b})
\end{aligned}$$

where $\boldsymbol{\tau}_2$ and $\boldsymbol{\tau}_{11}$ are

$$\begin{aligned}
\boldsymbol{\tau}_2 &= \eta_0\big[\boldsymbol{\nabla}\boldsymbol{v}_2 + (\boldsymbol{\nabla}\boldsymbol{v}_2)^\dagger\big] + \big(\eta_0^{\mathrm{b}} - \tfrac{2}{3}\eta_0\big)(\boldsymbol{\nabla}\cdot\boldsymbol{v}_2)\,\mathbf{1}\,, && (2.18\mathrm{a})\\
\boldsymbol{\tau}_{11} &= \big\langle\eta_1\big[\boldsymbol{\nabla}\boldsymbol{v}_1 + (\boldsymbol{\nabla}\boldsymbol{v}_1)^\dagger\big] + \big(\eta_1^{\mathrm{b}} - \tfrac{2}{3}\eta_1\big)(\boldsymbol{\nabla}\cdot\boldsymbol{v}_1)\,\mathbf{1}\big\rangle\,. && (2.18\mathrm{b})
\end{aligned}$$

Evidently, the force—in both the literal and the figurative sense of the word—behind the acoustic streaming $\boldsymbol{v}_2$ is the time-averaged products of first-order fields [13, 18]; thus, we define the acoustic body force as [8]

$$\hat{\boldsymbol{f}}_{\mathrm{ac}} = -\boldsymbol{\nabla}\cdot\big[\rho_0\langle\boldsymbol{v}_1\boldsymbol{v}_1\rangle - \boldsymbol{\tau}_{11}\big]\,. \qquad (2.19)$$

The boundary condition on $\boldsymbol{v}_2$ become [10, 19]

$$0 = \hat{\boldsymbol{n}}\cdot\big[\rho_0\boldsymbol{v}_2 + \langle\rho_1\boldsymbol{v}_1\rangle\big]\,, \qquad \text{at the fluid-solid boundaries.} \qquad (2.20)$$

The time-averaged products of two first-order fields, $\mathrm{Re}[A_1]$ and $\mathrm{Re}[B_1]$, may be calculated by $\langle\mathrm{Re}[A_1]\mathrm{Re}[B_1]\rangle = \frac{1}{2}\mathrm{Re}[A_1B_1^*]$, where the asterisk denotes complex conjugation [8].

2.5 The acoustic wave equation

We derive the acoustic wave equation starting from the first-order equations (2.14). First we recognize that the acoustic time-scale, $\tau_{\mathrm{osc}} \sim 0.1\,\mu\mathrm{s}$, is much shorter than that of heat diffusion, $\tau_{\mathrm{diff}} \sim l_{\mathrm{c}}^2/D^{\mathrm{th}} = 0.1\,\mathrm{s}$, where $l_{\mathrm{c}} \sim 0.1\,\mathrm{mm}$ is the length-scale of the system and $D^{\mathrm{th}} \sim 0.1 \times 10^{-6}\,\mathrm{m}^2\,\mathrm{s}^{-1}$ the thermal diffusivity. The diffusive term in Eq. (2.14a) may thus be neglected. Additionally, for small thermal gradients the advective term in Eq. (2.14b) becomes insignificant and may be neglected. The first-order equations thus become

$$\rho_0 c_p \partial_t T_1 - \alpha_p T_0 \partial_t p_1 = 0\,, \tag{2.21a}$$

$$\kappa_T \partial_t p_1 - \alpha_p \partial_t T_1 = -\boldsymbol{\nabla} \cdot \boldsymbol{v}_1\,, \tag{2.21b}$$

$$\rho_0 \partial_t \boldsymbol{v}_1 = -\boldsymbol{\nabla} p_1 + \eta_0 \nabla^2 \boldsymbol{v}_1 + \beta \eta_0 \boldsymbol{\nabla}\big(\boldsymbol{\nabla} \cdot \boldsymbol{v}_1\big)\,, \tag{2.21c}$$

where $\beta = \eta_0^{\mathrm{b}}/\eta_0 - 2/3$.

We eliminate $\partial_t T_1$ in Eq. (2.21b) using Eq. (2.21a) and differentiate this with respect to time as well as apply the divergence to get

$$\rho_0 \left(\kappa_T - \frac{T_0 \alpha_p^2}{\rho_0 c_p} \right) \partial_t^2 p_1 = \nabla^2 p_1 - (1+\beta)\eta_0 \nabla^2 (\boldsymbol{\nabla} \cdot \boldsymbol{v}_1)\,. \tag{2.22}$$

We then use Eq. (2.21b) to eliminate $\boldsymbol{v}_1$ in Eq. (2.22) and rewrite $\kappa_T - T_0\alpha_p^2/\rho_0 c_p$ to κ_s using Eqs. (2.8) and (2.7), whence we obtain the wave equation for the acoustic pressure with propagation speed $c_s = \sqrt{1/\rho_0 \kappa_s}$,

$$\frac{1}{c_s^2} \partial_t^2 p_1 = \left(1 + \frac{(1+\beta)\eta_0}{\rho_0 c_s^2} \partial_t \right) \nabla^2 p_1\,. \tag{2.23}$$

For a time-harmonic acoustic pressure field, Eq. (2.23) becomes the Helmholtz equation,

$$\nabla^2 p_1 = -k^2 p_1\,, \qquad \text{with } k = (1 + \mathrm{i}\Gamma) k_0\,, \tag{2.24}$$

where $k_0 = \frac{\omega}{c_s}$ is the wavenumber and $\Gamma = (1+\beta)\eta_0/2\rho_0 c_s^2$ a small damping coefficient. Inside a hard-walled rectangular box of width w and height h, the eigenmodes of Eq. (2.24) occur at the frequencies [13]

$$f_{n,m} = \frac{c_s}{2} \sqrt{\left(\frac{n}{w}\right)^2 + \left(\frac{m}{h}\right)^2}\,, \qquad \text{with } n, m = 0, 1, 2, \dots \tag{2.25}$$

Thus, a mode is characterized by its pair of integer indices n and m.

Chapter 3

Numerical simulation in COMSOL Multiphysics

This chapter concerns itself with the simulation software COMSOL Multiphysics 5.6. In Section 3.1, the finite element method for obtaining numerical solutions to partial differential equations (PDEs) is introduced. This is the numerical method employed by COMSOL to simulate physics-based systems. Then, in Section 3.2, the thermoviscous model presented in Section 2.4 is implemented in COMSOL, and in Section 3.3 a mesh convergence test is conducted to select a mesh.

3.1 The finite element method

The information presented in this section is obtained from a lecture note by Bruus [14].

3.1.1 The strong formulation of PDEs

Conservation laws are a recurring theme in physics. For this reason, many governing equations of physics take the same general form,

$$\boldsymbol{\nabla} \cdot \boldsymbol{J}\left[u(\boldsymbol{r}, t)\right] - F(\boldsymbol{r}, t) = 0\,, \ \text{for } \boldsymbol{r} \in \Omega\,, \tag{3.1}$$

where $\boldsymbol{J}$ is a generalized flux and F a generalized force driving said flux.

The form (3.1) is the strong formulation of a PDE on the domain Ω. The so-called *strong solutions* $u(\boldsymbol{r}, t)$ to Eq. (3.1) with specified boundary conditions on $\partial\Omega$ solve the problem exactly, on all of Ω. These solutions, however, are seldom obtainable analytically. Instead we seek *weak solutions* to the problems, which approximate the strong solutions on a discretized Ω.

3.1.2 Discretization of the computational domain

To discretize the domain Ω, a finite number N of points $\boldsymbol{r}_n$, $n = 1, 2, \ldots, N$ are selected from it. Then a mesh is developed using these as vertices for the mesh elements as shown for a triangular mesh in Fig. 3.1.

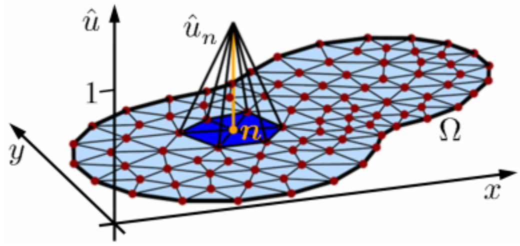

Figure 3.1: Illustration of a triangular mesh in the 2D domain Ω. It consists of the mesh vertices (red points), the mesh elements (light blue), the nth mesh cell (dark blue) with its center point $\boldsymbol{r}_n$ (yellow) and 1. order test function $\hat{u}_n$ (yellow line). Adapted from Ref. [14] with permission.

The node in $\boldsymbol{r}_n$ and its collection of mesh elements constitute the nth mesh cell. The nth mesh cell is associated with the test function $\hat{u}_n$, which is a piecewise but continuous polynomial of order p with compact support on the cell and which becomes unity in its node, $\boldsymbol{r}_n$. The set of test functions $\{\hat{u}_n\}_{n=1}^{N}$ constitutes a basis by which we can approximate the strong solutions,

$$u(\boldsymbol{r}) \approx \sum_{n=1}^{N} C_n^{(u)} \hat{u}_n(\boldsymbol{r})\,. \tag{3.2}$$

Here $C_n^{(u)}$ are unknown coefficients to be computed numerically.

3.1.3 The weak formulation of the PDE

Naturally, exchanging the strong solution for an approximate solution produces a non-zero defect,

$$d(\boldsymbol{r}) = \boldsymbol{\nabla} \cdot \boldsymbol{J}\left[u(\boldsymbol{r})\right] - F(\boldsymbol{r})\,. \tag{3.3}$$

By demanding that the projection of the defect on every basis function vanishes,

$$\int_{\Omega} \hat{u}_m(\boldsymbol{r}) \big\{ \boldsymbol{\nabla} \cdot \boldsymbol{J}[u(\boldsymbol{r})] - F(\boldsymbol{r}) \big\}\, \mathrm{d}V = 0, \quad \text{for } \boldsymbol{r} \in \Omega\,, \tag{3.4}$$

we obtain the *weak form* of Eq. (3.1) with a solution $u(\boldsymbol{r})$ of the form (3.2). For a linear flux operator, this is recast into a matrix problem for the unknown coefficients $C_n^{(u)}$,

$$K_{mn} C_n^{(u)} = F_m\,, \tag{3.5}$$

by defining the stiffness matrix K_{mn} and force vector F_m by

$$K_{mn} \equiv \int_{\Omega} \hat{u}_m(\boldsymbol{r}) \boldsymbol{\nabla} \cdot \boldsymbol{J}\left[\hat{u}_n(\boldsymbol{r})\right]\, \mathrm{d}V\,, \tag{3.6a}$$

and

$$F_m \equiv \int_\Omega \hat{u}_m(\boldsymbol{r}) F(\boldsymbol{r})\,\mathrm{d}V\,. \tag{3.6b}$$

Hence, the coefficients $C_n^{(u)}$ are determined by matrix inversion.

3.1.4 Imposing boundary conditions

Two types of boundary conditions are relevant to us in this study; they are the Neumann and Dirichlet boundary conditions. But to impose them, Eq. (3.4) requires a little more work. Applying the product rule of differentiation, $\hat{u}_m(\boldsymbol{\nabla}\cdot\boldsymbol{J}) = (\boldsymbol{\nabla}\hat{u}_m)\cdot\boldsymbol{J} - \boldsymbol{\nabla}\cdot(\hat{u}_m\boldsymbol{J})$, in conjunction with Gauss's theorem, $\int_\Omega \boldsymbol{\nabla}\cdot(\hat{u}_m\boldsymbol{J})\,\mathrm{d}V - \int_\Omega(\boldsymbol{\nabla}\hat{u}_m)\cdot\boldsymbol{J}\,\mathrm{d}V = \oint_{\partial\Omega}\hat{u}_m(\boldsymbol{n}\cdot\boldsymbol{J})\,\mathrm{d}A - \int_\Omega(\boldsymbol{\nabla}\hat{u}_m)\cdot\boldsymbol{J}\,\mathrm{d}V$, reveal the flux going across the boundary $\partial\Omega$,

$$\oint_{\partial\Omega}[\hat{u}_m\boldsymbol{n}\cdot\boldsymbol{J}]\,\mathrm{d}A + \int_\Omega[(-\boldsymbol{\nabla}\hat{u}_m)\cdot\boldsymbol{J} - \hat{u}_m F]\,\mathrm{d}V = 0\,. \tag{3.7}$$

Hence, a Neumann boundary condition is imposed by specifying $\boldsymbol{n}\cdot\boldsymbol{J}(\boldsymbol{r})$ in the integrand of the surface integral.

Any other type of boundary condition is written as $R\,[u(\boldsymbol{r},t),\boldsymbol{J}(\boldsymbol{r},t)] = 0$, and they are implemented by introducing the auxiliary field $\lambda(\boldsymbol{r})$ and its corresponding set of test functions $\{\hat{\lambda}_m\}_{m=1}^M$—the Lagrange multipliers—on the boundary. This turns Eq. (3.7) into

$$\oint_{\partial\Omega}\Big\{\hat{u}_m\lambda(\boldsymbol{r}) + \hat{\lambda}_m R[u(\boldsymbol{r},t),\boldsymbol{J}(\boldsymbol{r},t)]\Big\}\,\mathrm{d}A + \int_\Omega[(-\boldsymbol{\nabla}\hat{u}_m)\cdot\boldsymbol{J} - \hat{u}_m F]\,\mathrm{d}V = 0\,. \tag{3.8}$$

A Dirichlet boundary condition, then, is imposed by choosing $R\,[u(\boldsymbol{r},t),\boldsymbol{J}(\boldsymbol{r},t)] = u(\boldsymbol{r}) - D(\boldsymbol{r})$ and specifying $D(\boldsymbol{r})$, which is the desired value of $u(\boldsymbol{r})$ on the boundary. Accordingly—from its mathematical context in Eq. (3.8)—we infer that the auxiliary field $\lambda(\boldsymbol{r})$ is the surface flux that maintains the imposed value of $u(\boldsymbol{r})$ on the boundary.

3.2 Model implementation

The model presented in Section 2.4 is implemented in COMSOL using the software's PDE module. Here the governing equations (2.14) and (2.17) are specified in their weak forms by their generalized forces and fluxes; these are:

$$T_0: \quad \boldsymbol{J} = k_0^{\mathrm{th}}\boldsymbol{\nabla}T_0\,, \qquad F = 0\,, \tag{3.9a}$$

$$T_1: \quad \boldsymbol{J} = k_0^{\mathrm{th}}\boldsymbol{\nabla}T_1\,, \qquad F = \mathrm{i}\omega(\alpha_p T_0 p_1 - \rho_0 c_p T_1)\,, \tag{3.9b}$$

$$p_1: \quad \boldsymbol{J} = \boldsymbol{0}\,, \qquad F = \boldsymbol{\nabla}\cdot(\rho_0\boldsymbol{v}_1) - \mathrm{i}\omega\rho_0(\kappa_T p_1 - \alpha T_1)\,, \tag{3.9c}$$

$$\boldsymbol{v}_1: \quad \boldsymbol{J} = \boldsymbol{\tau}_1 - p_1\boldsymbol{1}\,, \qquad \boldsymbol{F} = \mathrm{i}\omega\rho_0\boldsymbol{v}_1\,, \tag{3.9d}$$

$$\boldsymbol{u}_1: \quad \boldsymbol{J} = \boldsymbol{\sigma}_1\,, \qquad \boldsymbol{F} = -\rho^{\mathrm{sl}}\omega^2(1+\mathrm{i}\Gamma^{\mathrm{sl}})^2\boldsymbol{u}_1\,, \tag{3.9e}$$

$$p_2: \quad \boldsymbol{J} = \rho_0\boldsymbol{v}_2 + \langle\rho_1\boldsymbol{v}_1\rangle\,, \qquad F = 0\,, \tag{3.9f}$$

$$\boldsymbol{v}_2: \quad \boldsymbol{J} = \boldsymbol{\tau}_2 - p_2\boldsymbol{1} - \rho_0\,\langle\boldsymbol{v}_1\boldsymbol{v}_1\rangle + \boldsymbol{\tau}_{11} \qquad \boldsymbol{F} = \boldsymbol{0}\,. \tag{3.9g}$$

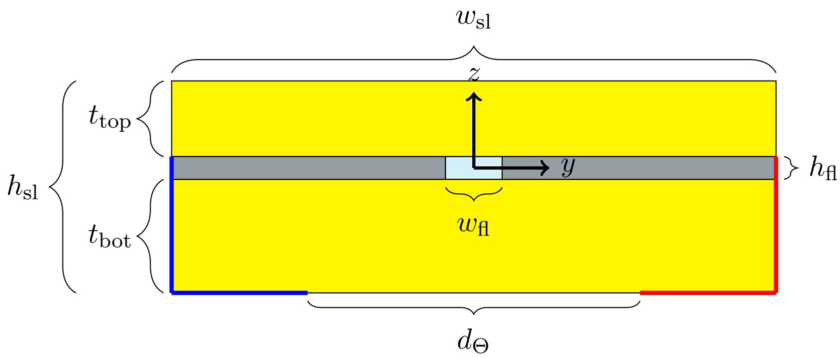

Figure 3.2: Sketch of the geometry. It depicts the yz-plane of a water-filled channel (light blue) going along the x-axis with silicon (gray) on its sides and pyrex glass (yellow) on its top and bottom. The red and the blue lines indicate where the system is heated and cooled, respectively, to produce a temperature gradient across the device. The dimensions are given in Table 3.1.

Table 3.1: Dimensions of the geometry in Fig. 3.2 [20].

w_{sl}	w_{fl}	h_{sl}	h_{fl}	t_{bot}	t_{top}	d_{Θ}	Units
4.0	0.375	1.4	0.15	0.75	0.50	2.2	mm

The geometry of the water-filled microchannel and surrounding solids is shown in Fig. 3.2; the dimensions are given in Table 3.1.

The boundary conditions are

$$T_0 = T_{\mathrm{a}} + \Delta T_0/2\,, \qquad \text{at every outer boundary if } \Delta T_0 = 0\,\mathrm{K}; \text{ otherwise, the red and blue lines in Fig. 3.2;} \tag{3.10a}$$

$$T_1 = 0\,, \qquad \text{same as the above;} \tag{3.10b}$$

$$\boldsymbol{v}_1 = -\mathrm{i}\omega(1+\mathrm{i}\Gamma^{\mathrm{sl}})\boldsymbol{u}_1\,, \qquad \text{at the fluid-solid boundaries;} \tag{3.10c}$$

$$\boldsymbol{u}_1 = d_0(y/w_{\mathrm{sl}} - 1/2)\hat{\boldsymbol{e}}_z\,, \qquad \text{at the bottom outer boundary;} \tag{3.10d}$$

$$\boldsymbol{\sigma}_1\cdot\hat{\boldsymbol{n}} = (\boldsymbol{\tau}_1 - p_1\mathbf{1})\cdot\hat{\boldsymbol{n}}\,, \qquad \text{at the fluid-solid boundaries;} \tag{3.10e}$$

$$\boldsymbol{\sigma}_1\cdot\hat{\boldsymbol{n}} = \mathbf{0}\,, \qquad \text{at the outer boundaries;} \tag{3.10f}$$

$$0 = \hat{\boldsymbol{n}}\cdot\big[\rho_0\boldsymbol{v}_2 + \langle\rho_1\boldsymbol{v}_1\rangle\big]\,, \qquad \text{at the fluid-solid boundaries.} \tag{3.10g}$$

Here $T_{\mathrm{a}} = 298\,\mathrm{K}$, $d_0 = 0.1\,\mathrm{nm}$, and, initially, $\Delta T_0 = 0\,\mathrm{K}$.

Note the actuation expression (3.10d): it contains both a symmetric term, $\frac{d_0}{2}$, and an anti-symmetric one, $d_0\frac{y}{w_{\mathrm{sl}}}$. This *asymmetric* mode of actuation ensures that every acoustic eigenmode, irrespective of its symmetry, can be excited.

In addition to the above conditions, it is necessary to fix the average of the second-order pressure p_2 by placing the following constraint on p_2:

$$\int_{\Omega_{\mathrm{fl}}} p_2\,\mathrm{d}y\mathrm{d}z = 0\,. \tag{3.10h}$$

This becomes necessary in order to attain numerical convergence because p_2 only enters the governing equations through its gradient $\boldsymbol{\nabla} p_2$.

The first-order equations are solved in the frequency domain, and the stationary second-order equations are solved using a stationary solver. This is carried out in three steps: (1) the zeroth-order thermal field is determined, fixing the zeroth-order water parameters; (2) the first-order fields are determined using the fully coupled approach, which achieves robustness at the expense of memory and time; and (3) the second-order time-averaged fields are determined, again using the fully coupled approach.

Prior to conducting a mesh convergence study, the maximum and the minimum mesh element size are set to $h_{\mathrm{xl}}^{\mathrm{max}} = \frac{h_{\mathrm{xl}}}{3}$ and $h_{\mathrm{xl}}^{\mathrm{min}} = 0.3 h_{\mathrm{xl}}^{\mathrm{max}}$, respectively, with x = s in the solids and x = f in the fluid. Additionally, boundary layer meshes are added at the interfaces between the solids and the fluid. The thickness of the initial layer in a domain is $0.5\,\delta_{\mathrm{t}}$ of the material in said domain, and the thickness of each subsequent layer is 1.3 times that of the preceding layer, for a total of 10 layers in the solids and 15 in the fluid. The thermal boundary layer thickness was chosen as the length scale for this because it was the shortest one of it, $\delta_{\mathrm{t}} \sim \sqrt{2D^{\mathrm{th}}/\omega} = 0.15\,\mathrm{\mu m}$, and the viscous one, $\delta_{\mathrm{s}} \sim \sqrt{2\eta_0/\rho_0\omega} = 0.40\,\mathrm{\mu m}$, in water.

3.3 Mesh convergence study

A mesh convergence study was conducted to ensure that simulation results are reliable and independent of the mesh. This was done by performing a parametric sweep of the mesh size and comparing each solution g of the sweep to a reference solution g_{ref} by

$$C(g) = \sqrt{\frac{\int_\Omega |g - g_{\mathrm{ref}}|^2 \,\mathrm{d}y\mathrm{d}z}{\int_\Omega |g_{\mathrm{ref}}|^2 \,\mathrm{d}y\mathrm{d}z}}\,. \tag{3.11}$$

The refinements made to the mesh in the sweep were controlled through a mesh refinement factor, 1/CONV, on the mesh element sizes. CONV was swept through values $1, 2, \ldots, 10$ with 10 thus corresponding to the most refined mesh of the sweep. The reference solution was the solution obtained using this mesh. A plot of $C(g)$ vs. CONV is shown in Fig. 3.3, which was produced with the actuation frequency $f = 1.96\,\mathrm{MHz}$.

As the mesh is made finer, the computing time increases. Sometimes the improved accuracy of the solutions from using a finer mesh does not outweigh the longer computing times. The mesh corresponding to CONV = 5 provides a solution with errors smaller than 1.0 percent of the reference solution and keeps the computing times relatively short (53 s, as against 2 min for CONV = 10). Thus, this mesh is employed from this point on, and each mesh element size and initial boundary layer thickness is 1/5 of its specified value in Section 3.2.

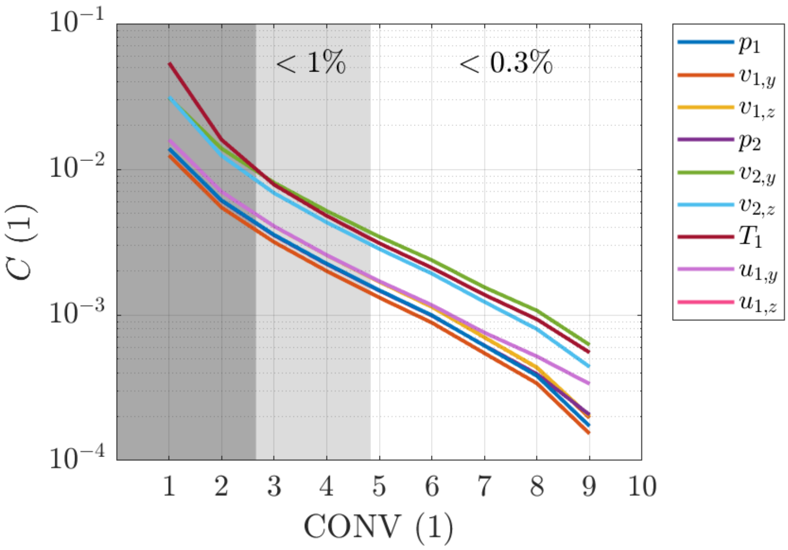

Figure 3.3: Semilog plot of the mesh convergence parameters C vs. the mesh refinement factor CONV. Exponential convergence is observed for CONV > 3. The shading in the background indicates the upper limit on the percentage error.

Chapter 4

Simulations without a temperature gradient

This chapter investigates the system described in Section 3.2 without an imposed temperature gradient. In Section 4.1, the resonance frequencies are determined for the horizontal half-wavelength (1,0), whole-wavelength (2,0), and vertical half-wavelength (0,1) eigenmodes from the time-averaged acoustic energy-density spectrum.[1] Then, in Section 4.2, an asymmetry in the acoustic streaming for the (1,0) mode, which is encountered in Section 4.1, is investigated. Finally, in Section 4.3, the performance of the device is evaluated for different placements of the microchannel. The chapter may come across as superficial, but it is short because it does not tie to the primary interest of this thesis directly.

4.1 Resonance analysis

Resonance frequencies are identified by large, narrow peaks in the time-averaged acoustic energy-density spectrum. This spectrum is obtained by performing a parametric sweep of the frequency to calculate the time-averaged acoustic energy-density, as given by [10, 21]

$$E^{\mathrm{ac}} = \frac{1}{4}\kappa_s |p_1|^2 + \frac{1}{4}\rho_0 |v_1|^2 \,, \tag{4.1}$$

for a range of frequencies and plotting the energy-density vs. the frequency.

A sweep was carried out in steps of $1.0 \times 10^{-4}\,\mathrm{MHz}$, producing the energy-density spectrum in Fig. 4.1. By these means, the resonance frequencies were determined to 4 decimals accuracy; they and other relevant parameters and quantities derived from Fig. 4.1 are given in Table 4.1. Of note, the Q-factors, which were calculated by $Q = \frac{f_{n,m}}{\Delta f}$ [18], are $\sim 10^3$, thus yielding $\epsilon \sim 10^{-4}$—well below unity.

The acoustic eigenmodes and streaming are shown in Fig. 4.2. For the most part, the eigenmodes in Fig. 4.2(a)–(c) appear as expected, except for an asymmetry in the vertical direction, which is present in all of them. In Fig. 4.2(d)–(e) the (1,0) and (2,0) streaming expectedly contain 4 and 8 stream rolls, respectively. The rolls, however, are

[1] The numbers in the parantheses are the integers n and m which characterize the different modes.

highly asymmetrical in both the vertical and horizontal directions, which, in Section 4.2, is found to be caused by the actuation (3.10d). Finally, the (0,1) streaming in Fig. 4.2(f) is a mess: it does not resemble the expected four stream rolls like Fig. 4.2(d) but along the sides of the channel. It appears to result from only actuating the system in the bottom.

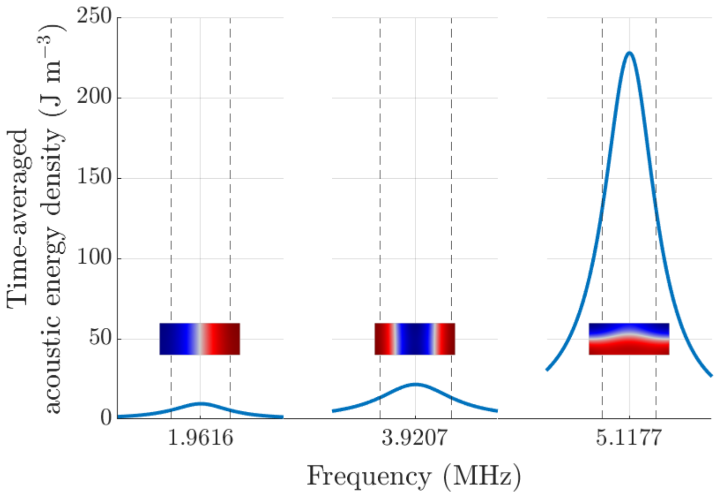

Figure 4.1: The time-averaged acoustic energy-density (4.1) vs. actuation frequency. The sweeps were conducted in steps of 1.0×10^{-4} MHz for intervals of 0.01 MHz around the resonance frequencies of the relevant eigenmodes, which are visualized by the superimposed images. The ticks on the Frequency-axis indicate the resonance frequencies; the dashed lines indicate the bounds of the full-width at half-maxes.

Table 4.1: Summary of the resonance frequencies, the full-width at half-maxes (FWHMs), the Q-factors, and the acoustic energy-densities of the $(1,0)$, $(2,0)$, and $(0,1)$ eigenmodes. The analytical (ana.) frequencies were calculated by the formula (2.25), while the other parameters and quantities were derived from Fig. 4.1.

Mode, (n,m)	Ana. frequency, $f^{\text{ana}}_{n,m}$ (MHz)	Num. frequency, $f^{\text{num}}_{n,m}$ (MHz)	Full-width at half-max, Δf (kHz)	Q-factor, Q (1)	Acous. energy-density, E^{ac} (J m^{-3})
(1,0)	2.0	1.9616	3.6	540	9.58
(2,0)	4.0	3.9207	4.3	910	21.6
(0,1)	5.0	5.1177	3.2	1600	228

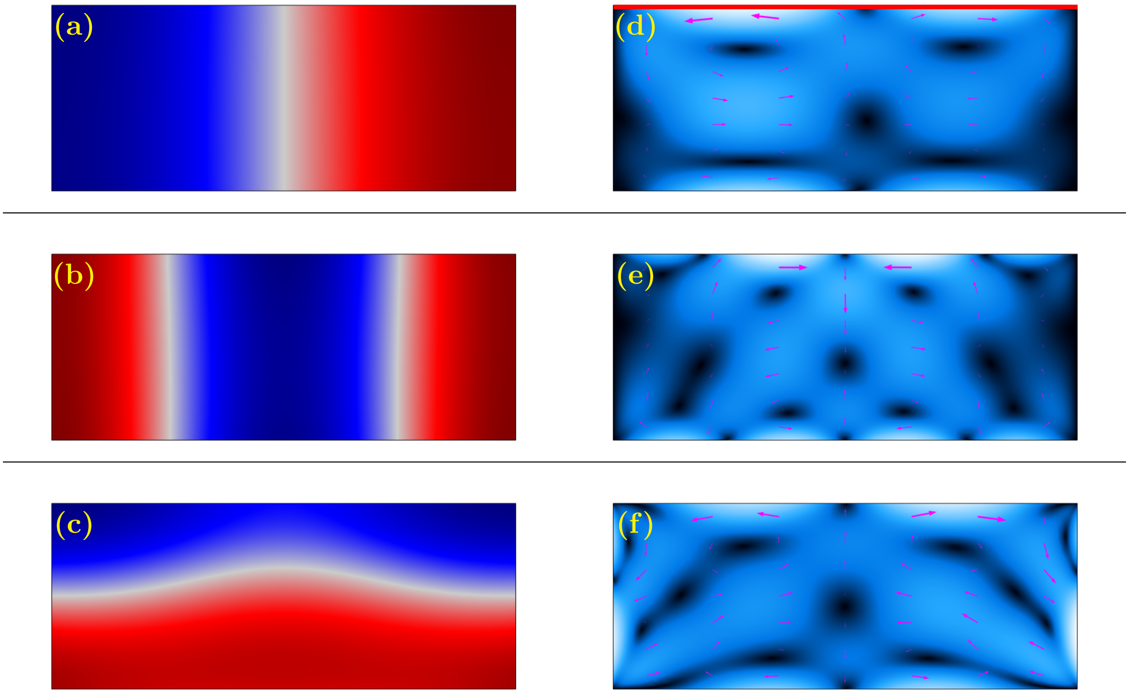

Figure 4.2: The acoustic eigenmodes, (a)–(c), and their respective acoustic streaming, (d)–(f), as indicated by the horizontal lines between the rows. Generally, colored lines in graphics indicate lines along which a quantity has been evaluated.

4.2 Acoustic streaming asymmetry

This is a short investigation of the asymmetry in the acoustic streaming, which was encountered in the previous section. As mentioned earlier, the cause to the asymmetries was the actuation (3.10d). Specifically, the asymmetric expression $\boldsymbol{d}_0 = d_0\big(\frac{y}{w_{\mathrm{sl}}} - \frac{1}{2}\big)\hat{\boldsymbol{e}}_z$ produced the horizontal asymmetry, while only actuating the system in the bottom produced the vertical one. The vertical asymmetry was foreseeable, but the horizontal one came as a surprise because the off-resonance modes supposedly are negligible compared to the resonance modes at resonance. For this short investigation, we focus on the (1,0) streaming in Fig. 4.2(d).

Since the acoustic body force $\langle \boldsymbol{\Pi} \rangle = \rho_0 \boldsymbol{\nabla} \cdot \langle \boldsymbol{v}_1 \boldsymbol{v}_1 \rangle$ is responsible for the stream rolls in the boundary layer which drive the stream rolls in the bulk [18], we inspect the body force. In Fig. 4.3, the horizontal component of the force $\langle \Pi \rangle_y / \rho_0 = \partial_y \langle v_{1,y} v_{1,y} \rangle + \partial_z \langle v_{1,z} v_{1,y} \rangle$ is evaluated along the red line in Fig. 4.2(d) at $3\,\delta_{\mathrm{s}}$ from the top of the channel. We find an asymmetry in the body force which emerges in the $\partial_z \langle v_{1,z} v_{1,y} \rangle$-term. Apparently, the asymmetric actuation produced a non-negligible symmetric term in $v_{1,z}$. Upon further investigation, the symmetric (+) term in $v_{1,z}$ was found to be $|v^+_{1,z}| = 2.1\,\mathrm{mm\,s^{-1}}$ contra

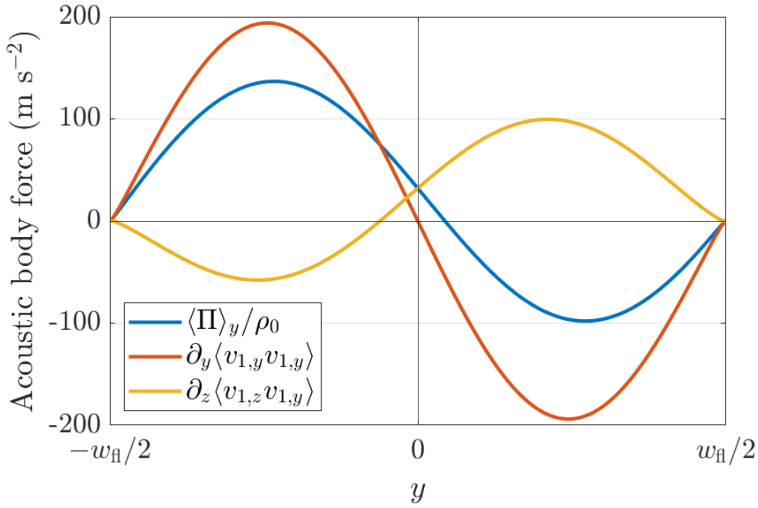

Figure 4.3: The horizontal component of the acoustic body force $\langle\Pi\rangle_y/\rho_0 = \partial_y\langle v_{1,y}v_{1,y}\rangle + \partial_z\langle v_{1,z}v_{1,y}\rangle$ evaluated along the red line in Fig. 4.2(d) at $3\,\delta_\mathrm{s}$ from the top of the channel. The two terms of the component are also plotted individually, revealing that the asymmetry emerges in the $\partial_z\langle v_{1,z}v_{1,y}\rangle$-term of the component.

the anti-symmetric $(-)$ one $|v_{1,z}^-| = 11\,\mathrm{mm\,s^{-1}}$; hence, they are comparable to each other. The $v_{1,z}^+$-term appeared to be enhanced by the off-center placement of the channel in the vertical direction. This was discovered by placing the channel in the center and subsequently observing that the asymmetry was reduced. The reason for this is related to the subject of the next section, so it is revealed there.

4.3 Microchannel placement investigation

The performance of the device is now investigated in relation to the placement of the microchannel. The performance is evaluated by measuring the acoustic energy-density of the system. The energy-density is relevant because it is related to the acoustic radiation force, which is used to manipulate microparticles [3]. The radiation force can be calculated from the potential U^rad by [21]

$$\boldsymbol{F}^\mathrm{rad} = -\boldsymbol{\nabla}U^\mathrm{rad}\,, \quad U^\mathrm{rad} = \frac{4\pi}{3}b^3\left(f_0\frac{1}{4}\kappa_\mathrm{fl}|p_1|^2 - f_1\frac{3}{8}\rho_\mathrm{fl}|v_1|^2\right)\,, \tag{4.2}$$

where f_0 and f_1 are monopole and dipole scattering coefficients, respectively.

In this numerical experiment, we define a reference position of the microchannel by the system described in Section 3.2. Every other channel placement is defined by a small displacement Δ of the channel relative to this reference position denoted by $\Delta = 0$. The channel was displaced by $\Delta y = \pm 50\,\mathrm{\mu m}$ along the y-axis or $\Delta z = \pm 20\,\mathrm{\mu m}$ along the z-axis. The resonance frequencies and corresponding acoustic energy-densities of the relevant eigenmodes for each channel placement are visualized in Fig. 4.4 and summarized in Tables 4.2 and 4.3, respectively.

For all three eigenmodes, the resonance frequencies were shifted to higher frequencies when the channel was moved down. The shifts, however, were typically small—about 0.1% relative to the reference frequencies—so further investigation of this is not imperative. Displacements in the horizontal direction did not produce any noticeable change to the resonance frequencies for any of the modes.

The resonance frequencies hardly changed, but the energy-densities certainly did. The energy-density was increased by 45% for the (1,0) mode in $-\Delta y$, but it was decreased by 50% in Δy. This was because the actuation (3.10d) resembled a hinge, which was fixed in $y = \frac{w_{\mathrm{fl}}}{2}$. The energy-density of (2,0) mode was less affected by it, but that of the (0,1) mode was reduced by 34% in Δy. When the hinge was removed, no difference between moving the channel to the right and moving it to the left was observed, as expected. In $-\Delta z$, the energy was increased for the (1,0) and (0,1) modes, while it was decreased for the (2,0) mode. In Δz, the opposite happened. This is consistent with Fig. 4.5 where we see that the strain in the solid increases beneath the channel for the (1,0) and (0,1) modes, but decreases for the (2,0) mode. Above the channel, however, the strain increased for the symmetric mode and decreased for the anti-symmetric one. This was the cause to the symmetric $v^{+}_{1,z}$-term being relatively large in the previous section and the reason that the asymmetry in the streaming was reduced, when the channel was moved downward.

Table 4.2: Summary of the resonance frequencies $f_{n,m}$ and relative frequency shifts $\delta f_{n,m} = \big(f_{n,m}^{(\Delta)} - f_{n,m}^{(0)}\big)/f_{n,m}^{(0)}$ of the (1,0), (2,0) and (0,1) eigenmodes for several placements of the microchannel. $\Delta = 0$ denotes the system described in Section 3.2, and $\pm\Delta y$ and $\pm\Delta z$ denote channel placements in the $\pm y$ and $\pm z$ directions relative to $\Delta = 0$ by $\Delta y = 50\,\mu\text{m}$ and $\Delta z = 20\,\mu\text{m}$.

Displacement, Δ	$f_{1,0}$ (MHz)	$\delta f_{1,0}$ ($\times 10^3$)	$f_{2,0}$ (MHz)	$\delta f_{2,0}$ ($\times 10^3$)	$f_{0,1}$ (MHz)	$\delta f_{0,1}$ ($\times 10^3$)
0	1.9616		3.9207		5.1177	
$-\Delta y$	1.959	−1.3	3.9203	−0.102	5.1204	0.5
$+\Delta y$	1.959	−1.3	3.9203	−0.102	5.1204	0.5
$-\Delta z$	1.9666	2.5	3.9211	0.102	5.1344	3.3
$+\Delta z$	1.9571	−2.3	3.9188	−0.4846	5.1084	−1.8

Table 4.3: Summary of the acoustic energy-densities $E_{n,m}^{\mathrm{ac},(\Delta)}$ and their relative differences $\delta E_{n,m}^{\mathrm{ac},(\Delta)} = \big(E_{n,m}^{\mathrm{ac},(\Delta)} - E_{n,m}^{\mathrm{ac},(0)}\big)/E_{n,m}^{\mathrm{ac},(0)}$ of the (1,0), (2,0), and (0,1) eigenmodes for several placements of the microchannel.

Displacement, Δ	$E_{1,0}^{\mathrm{ac}}$ ($\mathrm{J\,m^{-3}}$)	$\delta E_{1,0}^{\mathrm{ac}}$ (1)	$E_{2,0}^{\mathrm{ac}}$ ($\mathrm{J\,m^{-3}}$)	$\delta E_{2,0}^{\mathrm{ac}}$ (1)	$E_{0,1}^{\mathrm{ac}}$ ($\mathrm{J\,m^{-3}}$)	$\delta E_{0,1}^{\mathrm{ac}}$ (1)
0	9.56		21.6		228	
$-\Delta y$	13.9	0.451	21.8	0.0100	225	−0.0121
$+\Delta y$	4.77	−0.500	19.6	−0.0897	150	−0.341
$-\Delta z$	11.0	0.152	18.7	−0.132	249	0.0962
$+\Delta z$	8.02	−0.161	25.2	0.168	180	−0.210

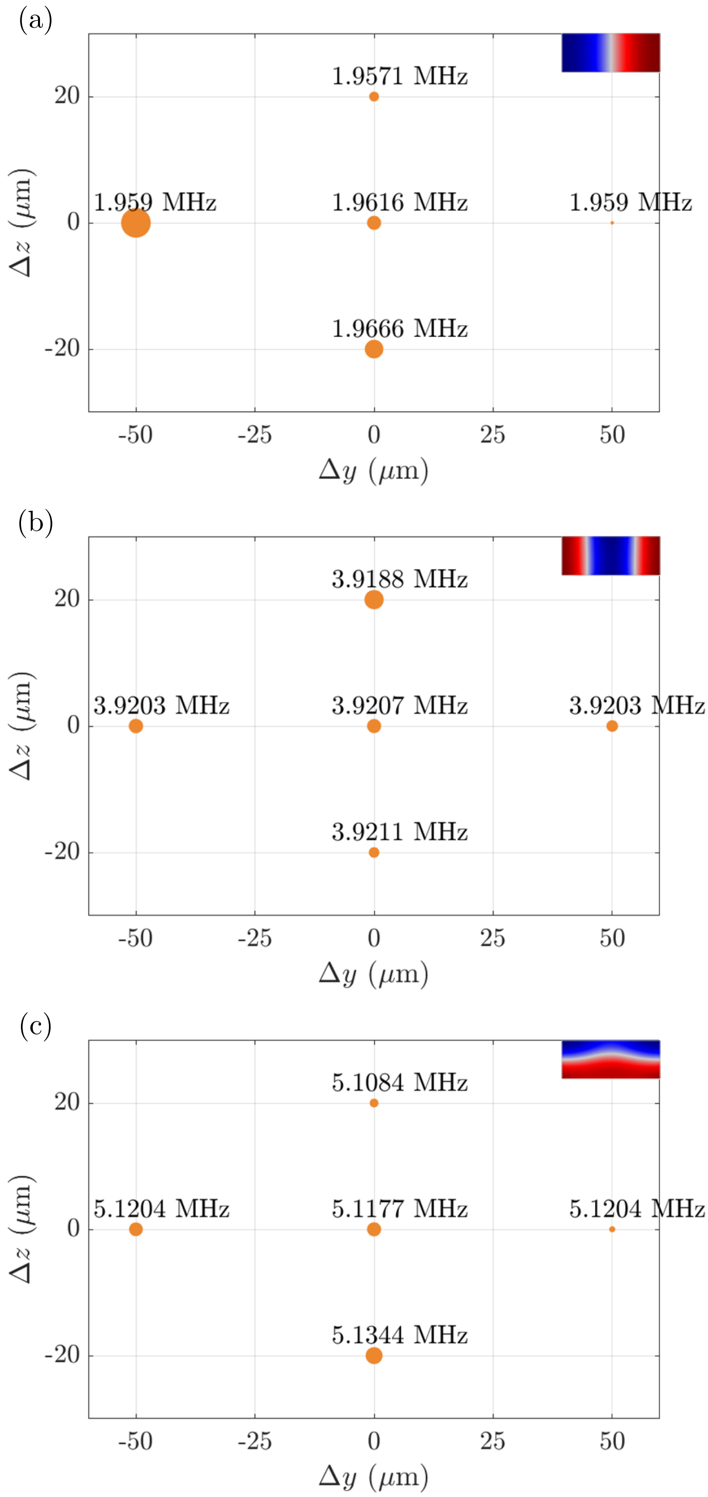

Figure 4.4: The resonance frequencies and acoustic energy-densities in relation to the placement of the microchannel. The reference placement is in the center, $(\Delta y, \Delta z) = (0, 0)$. The sizes of the points indicate the energy-density of the channel placement relative to that of the reference placement. The point sizes scale non-linearly to emphasize change.

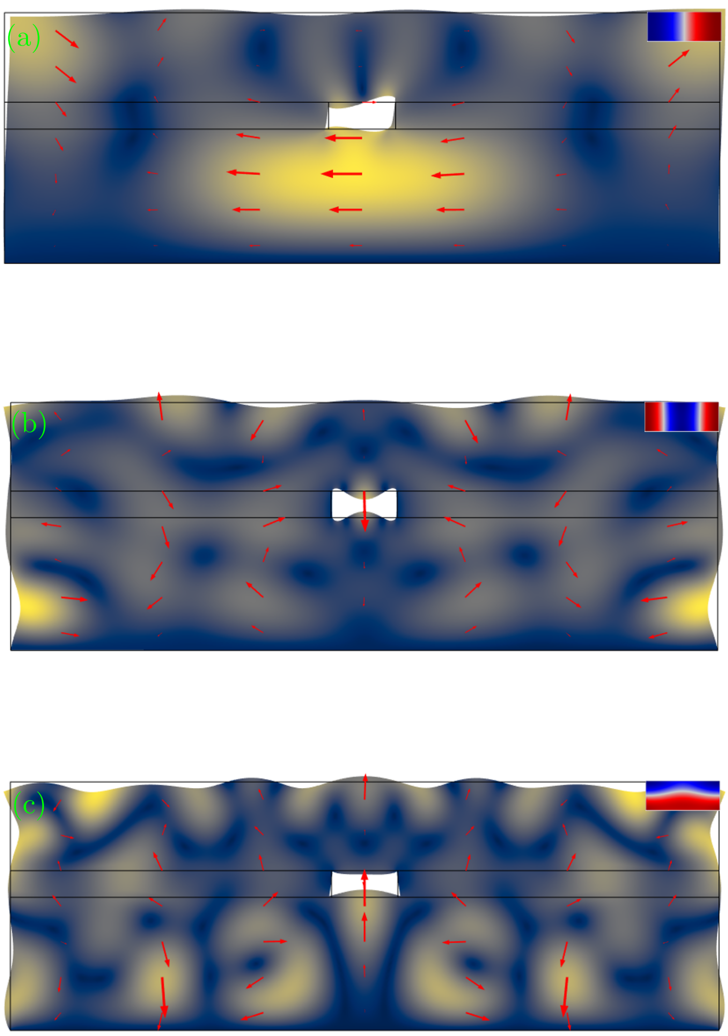

Figure 4.5: The displacement fields for the three eigenmodes indicated by the superimposed images in the graphics. Yellow signifies high amounts of strain, while black signifies low amounts. The red arrows represent the displacement vectors in different points.

Chapter 5

Simulations with a temperature gradient

In this chapter a horizontal temperature gradient is imposed across the device. First the system is investigated without acoustics in Section 5.1. Here a stationary flow establishes in presence of gravity because the density of the fluid varies across the channel width. In Section 5.2 the acoustics are turned on, and the effects of the temperature gradient on the acoustic streaming are investigated without gravity. The reason for neglecting gravity here is twofold: (1) the effects of gravity are small; and (2) mathematical consistency, as the fluid is assumed to be quiescent to zeroth order in the perturbation expansion (2.12). In Section 5.3 the velocity profile of the acoustic streaming with the temperature gradient is approximated for the (0,1) mode, and in Section 5.4 the prospect of using the temperature-gradient-influenced streaming to separate particles based on their contrast factors is discussed.

5.1 Temperature gradient without acoustics

Rayleigh-Bénard convection is an example of fluid motion driven by a temperature gradient. Here a confined fluid layer is heated from below which makes it rise upward by buoyancy, when the temperature difference between the bottom and top exceeds a critical value [22].

In our setup, a temperature gradient Θ is imposed in the horizontal direction instead. Under the influence of gravity, this system is not in hydrostatic equilibrium due to the horizontal density gradient arising from Θ. This is because the hydrostatic equation, $\boldsymbol{\nabla} p = \rho \boldsymbol{g}$, implies that the surfaces of constant density coincide with the equipotential surfaces of gravity [12]:[1]

$$\mathbf{0} = -\boldsymbol{\nabla}\rho \times \boldsymbol{\nabla}\Phi\,. \tag{5.1}$$

Here Φ is the gravitational potential defined by $\boldsymbol{g} = -\boldsymbol{\nabla}\Phi$.

[1] This is obtained by applying the curl to the hydrostatic equation, $\boldsymbol{\nabla} \times \big(\boldsymbol{\nabla} p - \rho \boldsymbol{g}\big) = \mathbf{0}$, and using that the curl of a gradient field is zero.

The condition (5.1) is not satisfied in the presence of Θ. Thus, the system is not in hydrostatic equilibrium and must have fluid motion. The simulation results of the system with the imposed temperature difference $\Delta T_0 = 1\,\mathrm{K}$ are shown in Fig. 5.1: in (a) we find that the temperature gradient is effectively confined to the water channel by the superior thermal conductivity of silicon compared to that of water; in (b) we see the fluid flow, which has a maximal magnitude of $U = 217\,\mathrm{nm\,s^{-1}}$, resulting from the temperature gradient.

The physical mechanism behind the fluid motion—I suspect—is the continuous jumping of the pressure in the horizontal direction due to a horizontal density gradient. Under this assumption, the pressure difference between y and $y + \mathrm{d}y$ is

$$\mathrm{d}p = -gz\mathrm{d}\rho = gz\rho_\mathrm{a}\alpha_p\Theta\mathrm{d}y\,, \tag{5.2}$$

where the last equality was obtained by applying the thermodynamic equation of state (2.9) (while neglecting the pressure-term due to its comparative smallness): $\mathrm{d}\rho = -\rho_\mathrm{a}\alpha_p\mathrm{d}T = -\rho_\mathrm{a}\alpha_p\Theta\mathrm{d}y$, where ρ_a is the fluid density at ambient temperature T_a. The pressure gradient in the horizontal direction thus becomes

$$\frac{\partial p}{\partial y} = \rho_\mathrm{a}\alpha_p\Theta g z\,. \tag{5.3}$$

Using this we estimate the velocity profile along the green line in Fig. 5.1(b) by a 1D pressure-driven channel flow [12], where a no-slip condition is applied in both $z = 0$ and $z = h_\mathrm{fl}/2$, and the pressure gradient is evaluated in[2] $z = h_\mathrm{fl}/4$. This yields

$$U = \frac{\rho_\mathrm{a}\alpha\Theta g z(2z - h_\mathrm{fl})h_\mathrm{fl}}{16\eta}\,. \tag{5.4}$$

On the grounds of Fig. 5.1(a), we assume that the temperature gradient is $\Theta = \frac{\Delta T_0}{w_\mathrm{fl}}$. The expression (5.4) has been plotted in Fig. 5.2 together with the numerical result. In it we find that the two resemble each other in magnitude, deviating only by 9.4%. However, using the numerical temperature gradient in the approximation lowers the approximation quite significantly. This is because heat escapes from the channel to the surrounding glass, as the conductivity of glass is similar to that of water. I also suspect some of the deviation occurs because the numerical temperature gradient is not entirely confined to the horizontal direction; hence, some buoyancy-driven flow do occur in the simulation, while the approximation assumes an entirely horizontal temperature gradient. Finally, the shape deviates, which—I assume—is because we try to estimate a 2D flow by a 1D calculation. It does not account for the vertical flow as well as the back-flow in the bottom, except for the no-slip condition in 0.

[2]This is the average of the pressure gradient between $z = 0$ and $z = h_\mathrm{fl}/2$.

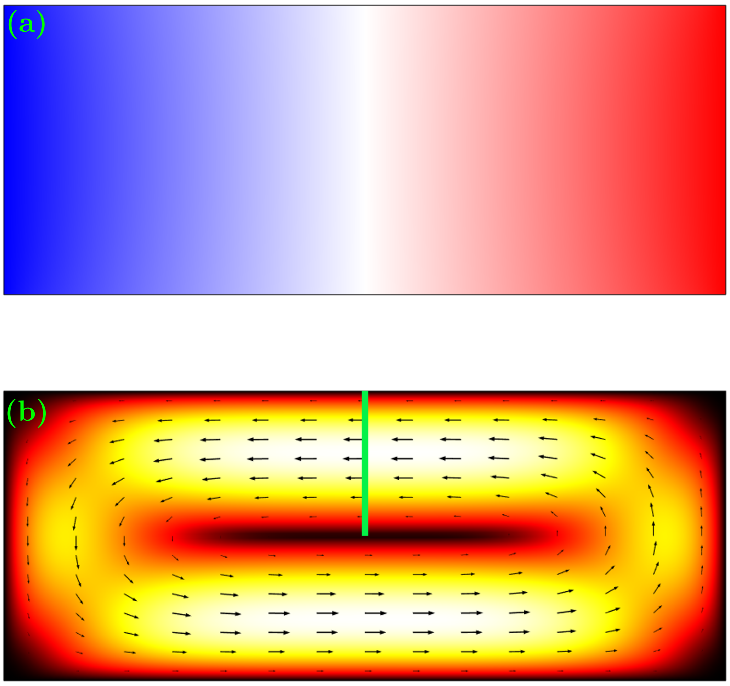

Figure 5.1: (a) The imposed temperature field which induces a horizontal density gradient. (b) The stationary flow which arises from the horizontal density gradient.

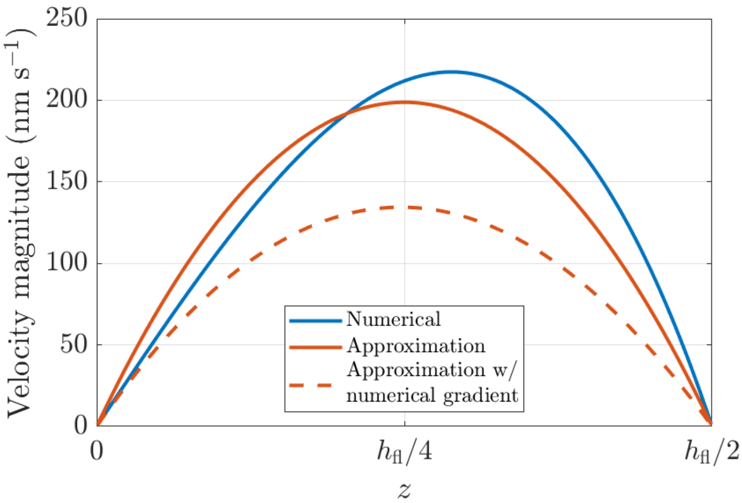

Figure 5.2: A comparison between the numerical result and the estimate (5.4) (using both $\Theta = \frac{\Delta T_0}{w_{\mathrm{fl}}}$ and the numerical gradient) along the green line in Fig. 5.1(b). Here “w/” is an abbreviation of “with”.

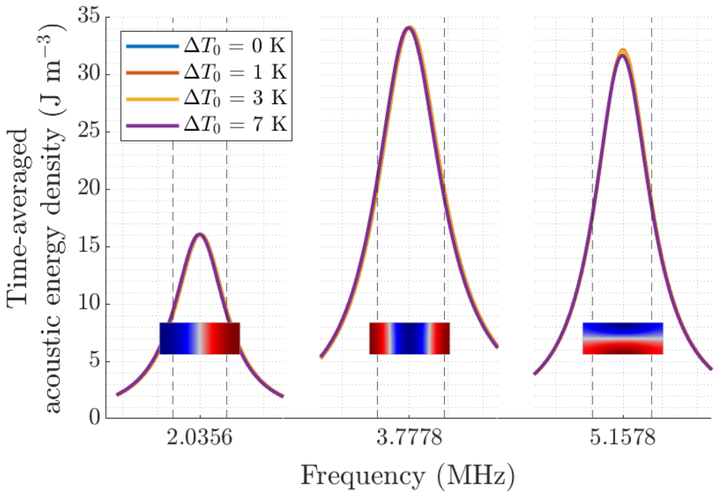

Figure 5.3: Time-averaged acoustic energy density vs. the actuation frequency with an imposed temperature difference ΔT_0 across the device. The system was actuated on both the top and bottom to produce the (1,0) and (0,1) eigenmodes and on both sides to produce the (2,0) mode.

5.2 Temperature gradient with acoustics

Starting from this section, both the acoustics and temperature gradient are present. In Chapter 4 we found that the geometry and means of actuation caused asymmetries in the acoustic streaming which, at worst, ruined the streaming. For this reason, we carry on with a system with $t_{\text{bot}} = t_{\text{top}} = 0.625\,\text{mm}$ and idealized actuations which take place on both the top and bottom of the system for the (1,0) and (0,1) eigenmodes and on both its sides for the (2,0) mode. The time-averaged acoustic energy-density spectrum was produced for this new system and actuation-strategy with an imposed temperature difference ΔT_0 across the device; that and the acoustic streaming are shown in Figs. 5.3 and 5.4, respectively. Compared to Fig. 4.2, the streaming in Fig. 5.4 without ΔT_0 look more like they should with four large rolls for every node in p_1. The (2,0) streaming, however, is weakened in its outermost stream rolls, and, underneath the (0,1) streaming, the streaming of another mode is present.

In Fig. 5.3, we find that imposing a temperature difference hardly affected the acoustic energy of the system—although, the energy did decrease marginally as ΔT_0 was increased. For this reason, I did not make any further inquiries into the spectrum. Regarding the streaming in Fig. 5.4, we do not observe any palpable differences between the streaming for the two horizontal modes, (1,0) and (2,0), with $\Delta T_0 = 1\,\text{K}$ and those without it. The vertical eigenmode (0,1), however, boasts a new streaming pattern for $\Delta T_0 = 1\,\text{K}$ where streaming occurs from left to right via the anti-nodes and returns via the node. This new streaming pattern emerges due to an acoustic body force density, described several times before [8, 23, 24], which arises from the gradients in the density and compressibility of

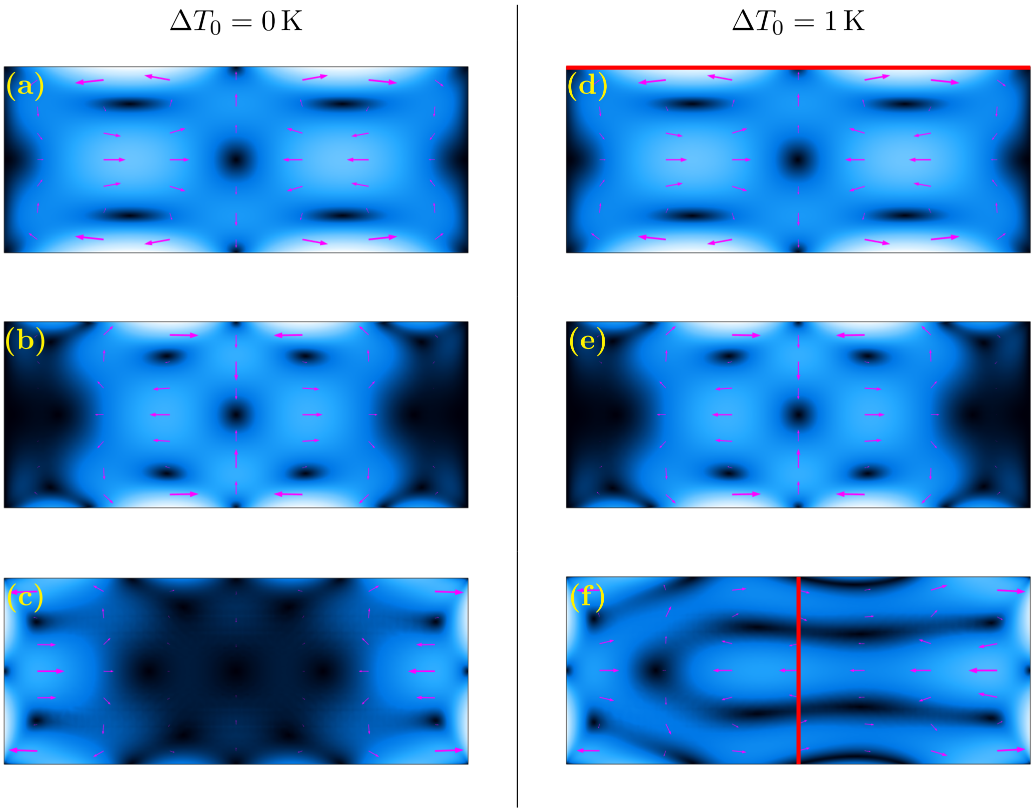

Figure 5.4: The acoustic streaming for the (1,0), (2,0), and (0,1) eigenmodes with $\Delta T_0 = 0\,\mathrm{K}$, (a)–(c), and $\Delta T_0 = 1\,\mathrm{K}$, (d)–(f). In (b) the outermost stream rolls are weakened, and in (c) the streaming of another mode is present underneath the (0,1) streaming.

an in-homogeneous fluid. For temperature-induced gradients, the experimentally verified expression for the acoustic body force acting on the bulk of the fluid is [8, 9]

$$\begin{aligned} \boldsymbol{f}_{\mathrm{ac}} &\approx -\frac{1}{4}|v_1|^2\boldsymbol{\nabla}\rho_0 - \frac{1}{4}|p_1|^2\boldsymbol{\nabla}\kappa_s \\ &= -\frac{1}{4}\left(a_\rho\rho_0|v_1|^2 + a_{\kappa_s}\kappa_s|p_1|^2\right)\alpha_p\boldsymbol{\nabla}T_0\,, \end{aligned} \tag{5.5}$$

where $a_q = \frac{(\partial \ln q/\partial T)_\rho}{\alpha_p}$ is the temperature sensitivity of the material parameter q.

Both the density and compressibility decrease with temperature, so the force (5.5) points in the direction of the high temperature region. The $|v_1|^2\boldsymbol{\nabla}\rho_0$-term is strongest in pressure nodes because the first-order bulk velocity field is related to the pressure field by [8] $\boldsymbol{v}_1 = -\boldsymbol{\nabla}\big(\mathrm{i}\frac{1-\mathrm{i}\Gamma_s}{\omega\rho_0}p_1\big)$, whereas the $|p_1|^2\boldsymbol{\nabla}\kappa_s$-term is strongest in anti-nodes. In view of this, the fact that the acoustic streaming toward the high temperature region in Fig. 5.4(f) occurs in the anti-nodes rather than the node indicates that $|p_1|^2\boldsymbol{\nabla}\kappa_s$ is the larger term of the two. Since $\kappa_s|p_1|^2 \sim p_\mathrm{e}^2/\rho_0 c_s^2$ and $\rho_0|v_1|^2 \sim k_0^2 p_\mathrm{e}^2/\rho_0\omega^2 = p_\mathrm{e}^2/\rho_0 c_s^2$, it becomes a matter of which material parameter, ρ_0 or κ_s, is more sensitive to a temperature change than the other. The compressibility is 10 times more temperature sensitive than the density[3], so $|p_1|^2\boldsymbol{\nabla}\kappa_s$ becomes the dominant term.

The velocity profile of the horizontal component $v_{2,y}$ of the acoustic streaming in Fig. 5.4(f) is shown in Fig. 5.5. An outflow from the high temperature region can be observed in the pressure node. This is water being expelled to maintain the steady stream of fluid by making space for it. As it cannot pass through the wall in $y = \frac{w_\mathrm{fl}}{2}$, it leaves in the pressure node where the acoustic body force (5.5) is weaker than anywhere else. The streaming between the high and low temperature regions is significant because particles are potentially displaced by a Stokes drag which is exerted on them by the streaming. Particles which are suspended via acoustophoresis or other such processes will experience a drag force in the direction of low temperature region in the node and high temperature region in the anti-nodes. This is further discussed in Section 5.4.

In Fig. 5.5(b), we see that the maximal outflow velocity increases linearly with the imposed temperature difference ΔT_0. This is not surprising because the temperature gradient $\boldsymbol{\nabla}T_0$ enters the equations linearly through the acoustic body force which drives the inflow to the high temperature region and mass conservation requires that $\int v_{2,y}\,\mathrm{d}z \approx U_\mathrm{in}^\mathrm{avg} l_\mathrm{in} - U_\mathrm{out}^\mathrm{avg} l_\mathrm{out} = 0$, implying that $U_\mathrm{out}^\mathrm{avg} = \frac{l_\mathrm{in}}{l_\mathrm{out}} U_\mathrm{in}^\mathrm{avg}$. We can determine the ratio $\frac{l_\mathrm{in}}{l_\mathrm{out}}$ by first locating the interfaces between the inflows and outflow. These are found numerically—later analytically—in $z = \pm a$ where $a \approx 32\,\mathrm{\mu m}$. Hence, we compute $\frac{l_\mathrm{in}}{l_\mathrm{out}} = \frac{h_\mathrm{fl}-2a}{2a} = 1.3$, and so $U_\mathrm{out}^\mathrm{avg}/U_\mathrm{in}^\mathrm{avg} = 1.3$, which also is verified by comparing the streaming magnitudes in the simulations. Mass conservation thus explains why the outflow magnitude both increases linearly with ΔT_0 and is greater than that of the individual inflows.

We can make a coarse estimate of the inflow velocity magnitude by balancing the acoustic body force on the fluid with frictional force of viscosity. If we neglect the $|v_1|^2\boldsymbol{\nabla}\rho_0$-

[3]The temperature sensitivities of several parameters are summarized in Table A.1 in Appendix A.

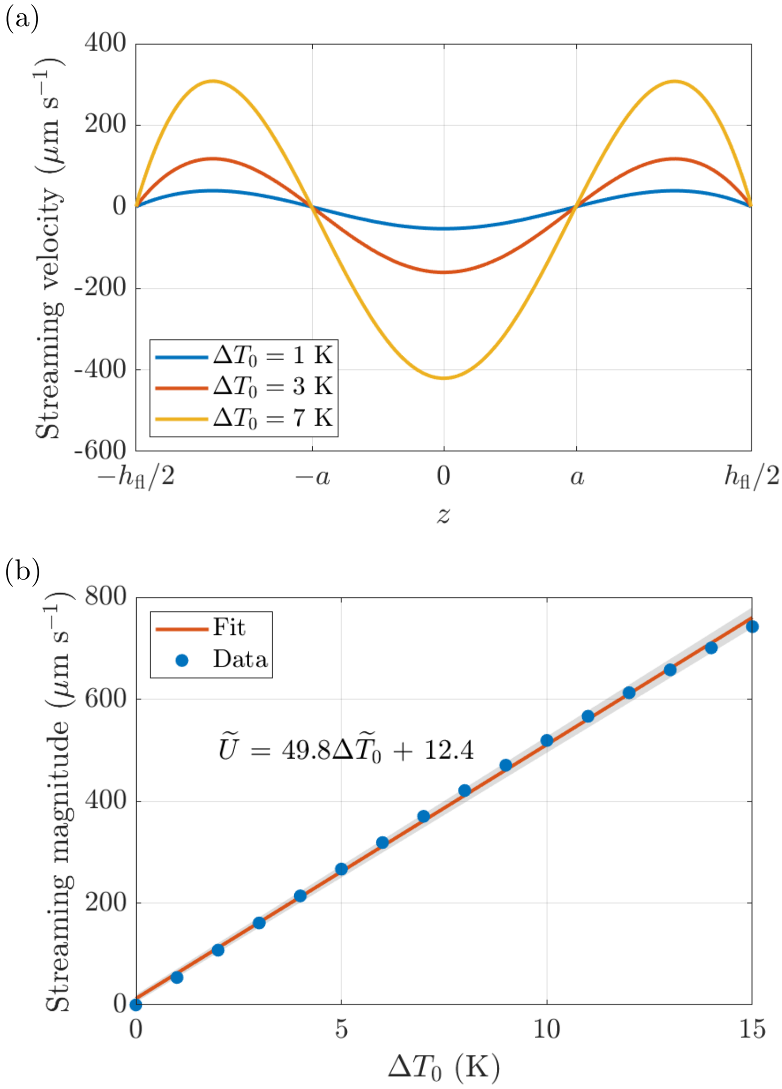

Figure 5.5: (a) Velocity profiles of the horizontal acoustic streaming induced by the acoustic body force (5.5) with different ΔT_0. It was evaluated along the red line in Fig. 5.4(f) at $y = 0$. The interfaces between the inflows to the high temperature region and the outflow to the low temperature one are located in a. (b) The maximal outflow velocity vs. the imposed temperature difference. The gray shading around the fit indicates the 95% confidence interval of the fit. Quantities with tildes are non-dimensionalized, e.g., $\Delta\widetilde{T}_0 = \Delta T_0/1\,\mathrm{K}$.

term in Eq. (5.5) and assume that $\partial_z \sim \frac{2}{h_{\mathrm{fl}}}$, then for $\Delta T_0 = 1\,\mathrm{K}$ we get

$$U_{\mathrm{in}} \sim -\frac{1}{4}\frac{a_{\kappa_s}\kappa_s\alpha_p\Theta p_{\mathrm{a}}^2 h_{\mathrm{fl}}^2}{4\eta_0} \approx 2.4\,\mathrm{mm\,s^{-1}}\,. \tag{5.6}$$

Compared to the number $39\,\mathrm{\mu m\,s^{-1}}$ from the simulations, this greatly overestimates the magnitude. The biggest culprit behind this is perhaps the disregard of a pressure gradient acting against the body force related to the outflow. Also, the viscous dissipation is underestimated because the shear strains in the fluid are smaller without the outflow than with it, and thus the velocity is overestimated. A better estimate is obtained in Section 5.3 where the outflow is taken into account.

Although the acoustic streaming for the horizontal eigenmodes, (1,0) and (2,0), appear unaffected by the acoustic body force (5.5), the streaming magnitudes for both modes increase in the high temperature region and decrease in the low temperature one. The streaming magnitude was evaluated in $(y, z) = (\pm w_{\mathrm{fl}}/4, 0)$ and plotted against ΔT_0 for the (1,0) mode, which is shown in Fig. 5.6(a). It is surprising because the acoustic body force (5.5) points in the opposite direction of the streaming in the high temperature region and in the same direction as the streaming in the low temperature one. By investigating the horizontal component of the body force $\boldsymbol{\nabla}\cdot\langle\rho_0\boldsymbol{v}_1\boldsymbol{v}_1\rangle$ in $3\,\delta_{\mathrm{s}}$ from the top of the channel, Fig. 5.6(b), we find a skewing in the force which is also present in the first-order velocity field, Fig. 5.6(c). I found that the speed of sound c_s was largely responsible for the skewing as setting c_s to a constant reduced the skewing significantly. This is supported by the fact that $a_{c_s} = \frac{(\partial \ln c_s/\partial T)_\rho}{\alpha_p} = -\frac{a_{\kappa_s}+a_{\rho_0}}{2} = 5.5$; hence, c_s is more temperature sensitive than the density. Using the results of the simulation, the ratio was determined by evaluating $\left|\frac{\Delta c_s/c_s}{\Delta\rho_0/\rho_0}\right|$ yielding ≈ 6.7. Otherwise, this part remains inconclusive.

5.3 Streaming approximation

To describe the acoustic streaming induced by the body force (5.5) in Fig. 5.4(f), we approximate its velocity profile along the red line in the figure. We consider the water-filled channel in the yz-plane, which is assumed *wide*. The temperature gradient $\boldsymbol{\nabla}T_0 = \Theta\hat{\boldsymbol{e}}_y$ and standing acoustic wave $p_{\mathrm{ac}} = p_{\mathrm{e}}\sin(k_0 z)$ with $k_0 = \frac{\pi}{h_{\mathrm{fl}}}$ give rise to the acoustic body force[4] $\boldsymbol{f} = -\frac{F}{2}\big[1-\cos(2k_0 z)\big]\hat{\boldsymbol{e}}_y$ with $F = \frac{1}{4}a_{\kappa_s}\kappa_s\alpha_p\Theta p_{\mathrm{e}}^2$, which drives the steady stream of fluid along the width of the channel. Due to the assumed "wideness" of the channel and the fact that $\boldsymbol{f}$ is a function of z only, we assume the following form of the velocity field: $\boldsymbol{U} = U_y(z)\hat{\boldsymbol{e}}_y$.[5] This implies that $\boldsymbol{\nabla}\cdot\boldsymbol{U} = 0$ and $(\boldsymbol{U}\cdot\boldsymbol{\nabla})\boldsymbol{U} = \boldsymbol{0}$, and the Navier–Stokes equation becomes

$$\frac{\partial p}{\partial y} = \eta_0\frac{\mathrm{d}^2 U_y}{\mathrm{d}z^2} - \frac{F}{2}\big[1-\cos(2k_0 z)\big]\,, \tag{5.7a}$$

$$\frac{\partial p}{\partial z} = 0\,. \tag{5.7b}$$

[4]The squared sine function was rewritten using the trigonometric identity $\sin^2(x) = \frac{1}{2}[1-\cos(2x)]$.

[5]If $\partial_y \sim 1/w_{\mathrm{fl}}$, then we find that $\partial_y \to 0$ in the limit $w_{\mathrm{fl}} \to \infty$. Hence, $\boldsymbol{U}$ effectively becomes independent of y.

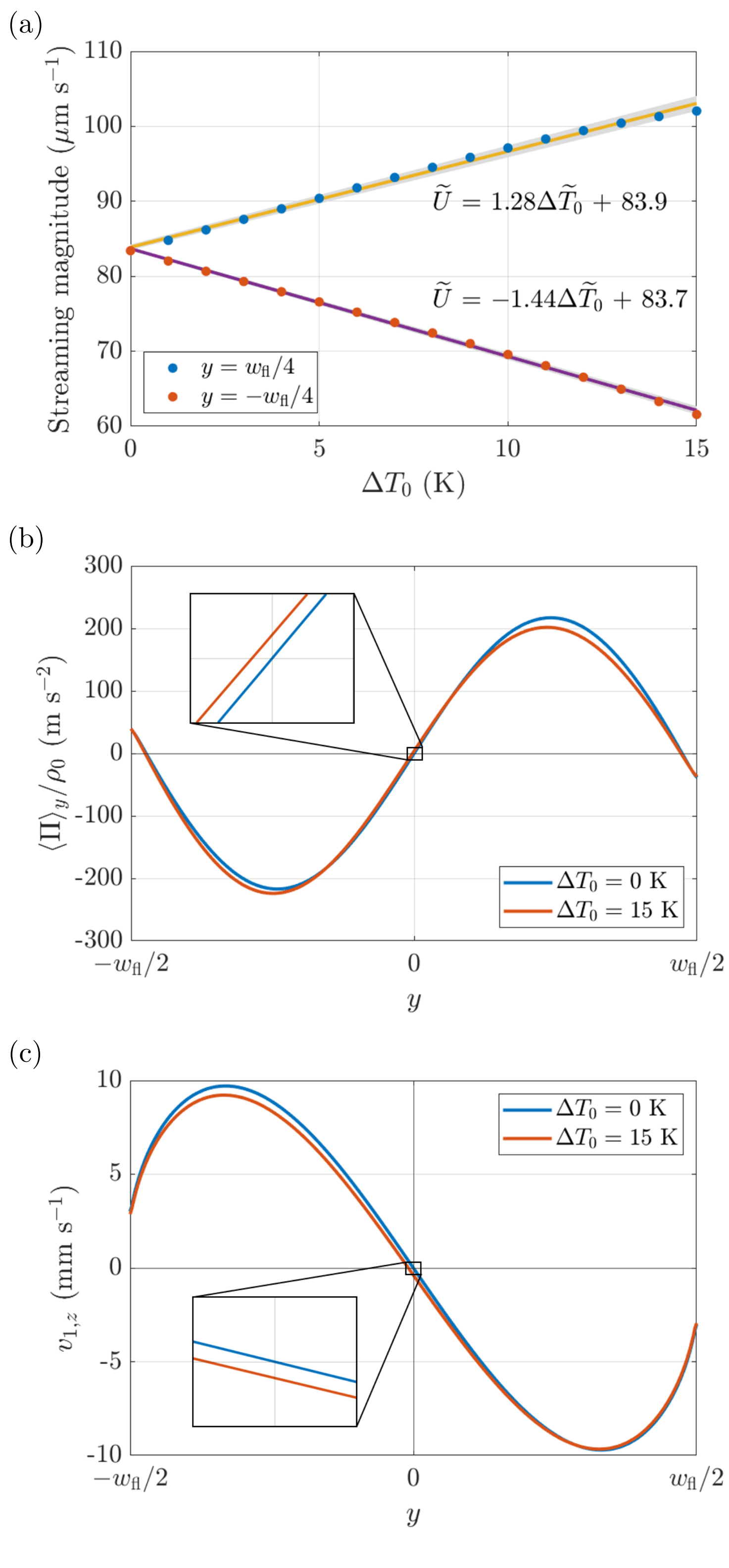

Figure 5.6: (a) Streaming magnitude for the (1,0) mode vs. imposed temperature difference. (b) The horizontal component of $\boldsymbol{\nabla} \cdot \langle \rho_0 \boldsymbol{v}_1 \boldsymbol{v}_1 \rangle$ evaluated along the red line in Fig. 5.4(d) at $3\,\delta_\mathrm{s}$ from the top of the channel. (c) The vertical velocity component $v_{1,z}$ along the same line as before.

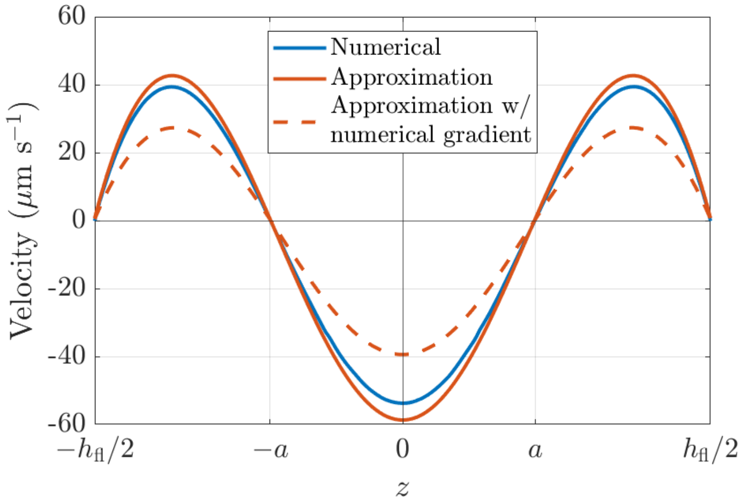

Figure 5.7: Velocity profile of the horizontal acoustic streaming induced by the acoustic body force (5.5) for the (0,1) mode with $\Delta T_0 = 1\,\mathrm{K}$. The numerical profile was evaluated along the red line in Fig. 5.4(f) at $y = 0$.

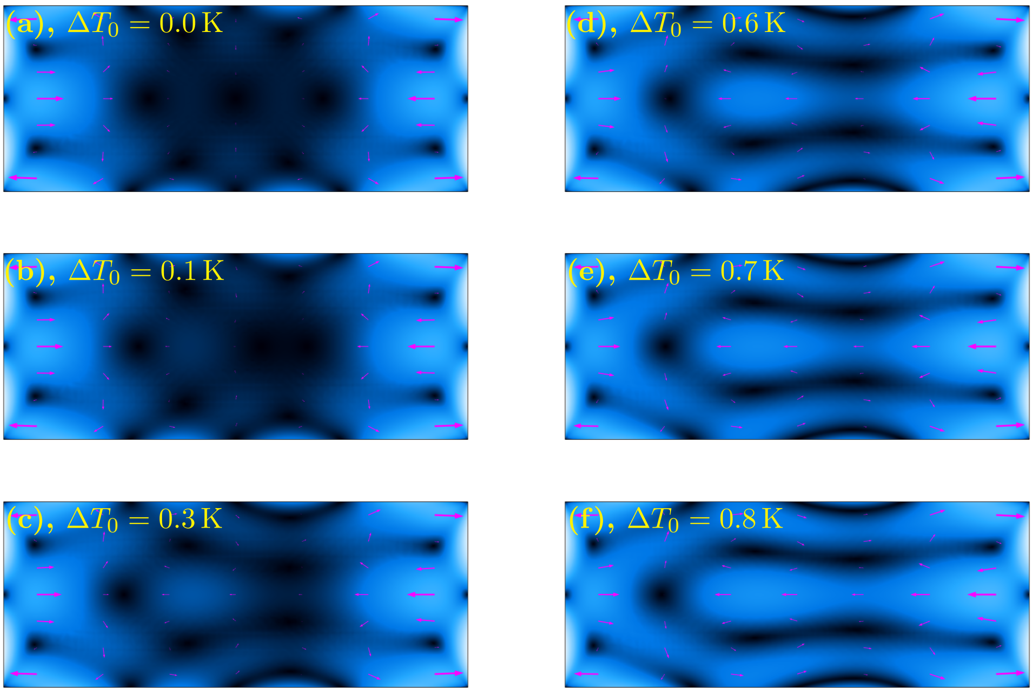

Figure 5.8: The acoustic streaming for the (0,1) mode with different imposed temperature differences ΔT_0 across the device.

From Eq. (5.7), it follows that $\boldsymbol{\nabla} p = G\hat{\mathbf{e}}_y$ where G is a constant; hence, the problem reduces to a single ordinary differential equation,

$$\eta_0 \frac{\mathrm{d}^2 U_y}{\mathrm{d}z^2} = \frac{F}{2}\big[1 - \cos(2k_0 z)\big] + G\,, \quad U_y(\pm h_{\mathrm{fl}}/2) = 0\,. \tag{5.8}$$

Here G is determined by a no-discharge rate condition,

$$\int_{-\frac{h_{\mathrm{fl}}}{2}}^{\frac{h_{\mathrm{fl}}}{2}} U_y \,\mathrm{d}z = 0\,, \tag{5.9}$$

which is imposed because the fluid cannot pass through the walls of the channel in $y = \pm\frac{w_{\mathrm{fl}}}{2}$.

To solve Eq. (5.8), we integrate it twice and apply the no-slip condition,

$$U_y = \frac{2F\cos(2\pi z/h_{\mathrm{fl}})h_{\mathrm{fl}}^2 - (h_{\mathrm{fl}} - 2z)(h_{\mathrm{fl}} + 2z)(F + 2G)\pi^2 + 2Fh_{\mathrm{fl}}^2}{16\eta_0\pi^2}\,. \tag{5.10}$$

Using this in Eq. (5.9) yields an expression for G,

$$G = -\frac{F}{2}\left(\frac{\pi^2 - 3}{\pi^2}\right) \approx -0.35F\,. \tag{5.11}$$

This is inserted into Eq. (5.10), yielding the profile

$$U_y = U_0\left[2\cos\left(\frac{2\pi}{h_{\mathrm{fl}}}z\right) + 12\left(\frac{z}{h_{\mathrm{fl}}}\right)^2 - 1\right]. \tag{5.12}$$

where $U_0 = \frac{F}{\eta_0}\left(\frac{h_{\mathrm{fl}}}{4\pi}\right)^2$ is the outflow streaming magnitude.

As seen in Fig. 5.7, the analytical expression for the horizontal streaming profile compares reasonably well to the numerical one. It overestimates the streaming, but this can partly be attributed to the $|v_1|^2\boldsymbol{\nabla}\rho_0$-term in Eq. (5.5), which was disregarded: the term would have constituted 1/11 of the total body force and impeded the outflow from the high temperature region to the low temperature one and consequently slowed down the streaming everywhere. The largest deviation from the numerical result occurred in $z = 0$ with 9%. This error was reduced to 4% by making the density constant in the simulation, which effectively removed $|v_1|^2\boldsymbol{\nabla}\rho_0$-term in the body force. Unfortunately, using the numerical temperature gradient lowers the predicted streaming even more. The same thing occured in Section 5.1, and so perhaps it is the disregard of the y-dimension causing the discrepancy because $\partial_y \sim \frac{1}{w_{\mathrm{fl}}}$ and $w_{\mathrm{fl}} \sim h_{\mathrm{fl}}$, and thus $\partial_y v_y \neq 0$. This, however, is conjecturing.

An analytical expression for the slope in Fig. 5.5(b) can be obtained by simply evaluating Eq. (5.12) in $z = 0$ and using that $\Theta \approx \frac{\Delta T_0}{w_{\mathrm{fl}}}$,

$$\left|\frac{U_0}{\Delta T_0}\right| = \left|\frac{a_{\kappa_s}\kappa_s\alpha_p p_{\mathrm{e}}^2 h_{\mathrm{fl}}^2}{64\pi^2 w_{\mathrm{fl}}\eta_0}\right| = 58.7\,\mathrm{\mu m\,s^{-1}\,K^{-1}}\,. \tag{5.13}$$

This deviates from the numerical result by 17%; however, as just mentioned, the approximation (5.12) neglects the density-term in the acoustic body force, which would have slowed down the streaming. Also, using the numerical temperature gradient lowers the slope significantly, but it does not make the analytical slope better.

In the interfaces between the inflows to the high temperature region and the outflow to the low temperature one, the velocity is zero. Hence, the interfaces are located in the points $z = \pm a$ where the forces on the fluid are balanced:

$$\frac{F}{2}\big[1-\cos(2k_0 a)\big] = -G\,. \tag{5.14}$$

Solving the above equation for a yields

$$a = \frac{\arccos(3/\pi^2)}{2\pi} h_{\mathrm{fl}} = 30\,\mathrm{\mu m}\,, \tag{5.15}$$

which only deviate from the numerical result by 6%. The deviation, however, appeared to be related to the finite spatial resolution of the simulation as well as its limited precision, because when a was determined from the approximation evaluated within COMSOL, the analytical approximation predicted the same as the numerical result. Note also that Eq. (5.15) is independent of the force magnitude F, as is observed in Fig. 5.5(a).

The characteristic rolls in the bulk, as seen in Fig. 5.4(e), are driven by small rolls inside the boundary layer [18]. The small rolls produce a pressure in the bulk [18] $p_2 = -\frac{3}{2c_s}u_0^2\cos(2k_0 z)\eta_0 k_0 \mathrm{e}^{-2k_0 y}$ with $u_0 = \frac{p_e}{\rho_0 c_s}$, which is negative in the anti-nodes of the acoustic wave. This pressure maintains the large stream rolls in the low temperature region, while the body force density $\frac{F}{2}[1-\cos(2k_0 z)]+G$ drives the streaming away to the high temperature one. The onset of the streaming between the low and high temperature regions should thus occur when the body force density equals the pressure gradient $\partial p_2/\partial y$ in an anti-node, i.e., in $z = \pm h_{\mathrm{fl}}/2$:

$$-\frac{3\eta_0}{c_s^3}\left(\frac{p_e k_0}{\rho_0}\right)^2 \mathrm{e}^{-2k_0 y} = F + G\,. \tag{5.16}$$

An upper bound on Θ is obtained by evaluating the above in $y = 0$ and solving for Θ:

$$\Theta_0 = -\frac{24\pi^4\eta_0}{a_{\kappa_s}\alpha_p c_s \rho_0 h_{\mathrm{fl}}^2(\pi^2+3)} = 1.87\,\mathrm{K\,mm^{-1}}\,. \tag{5.17}$$

Computing the corresponding temperature difference, $\Delta T = \Theta_0 w_{\mathrm{fl}}$, yields 0.7 K. In Fig. 5.8 the onset of the streaming due to the body force density is shown. Already at $\Delta T_0 = 0.3\,\mathrm{K}$ a streaming between the low and high temperature regions is observed; however, there is hardly any outflow from the high temperature region, suggesting that the streaming between the two regions is weak.

5.4 Separation using the imposed streaming

As mentioned in Section 5.2, the acoustic streaming induced by the acoustic body force (5.5) will exert a Stokes drag force on the particles suspended in the liquid. Often, particles are suspended via acoustophoresis where the acoustic radiation force (4.2) moves them to a node or an anti-node of the acoustic wave, depending on the scattering coefficients $f_0(\kappa_\mathrm{p})$ and $f_1(\rho_\mathrm{p})$, where κ_p and ρ_p are the compressibilities and densities of the particles, respectively [21]:

$$f_0 = 1 - \frac{\kappa_\mathrm{p}}{\kappa_\mathrm{fl}}, \quad f_1 = \frac{2(\rho_\mathrm{p} - \rho_\mathrm{fl})}{2\rho_\mathrm{p} + \rho_\mathrm{fl}}. \tag{5.18}$$

For the acoustic wave $p_1 = p_\mathrm{e}\sin(k_0 z)$ and corresponding velocity field $\boldsymbol{v}_1 = -\mathrm{i}\frac{p_\mathrm{e}}{\rho_0 c_s}\cos(k_0 z)\hat{\boldsymbol{e}}_z$, the radiation force (4.2) on a particle of radius b becomes

$$\boldsymbol{F}^\mathrm{rad} = 4\pi b^3 E^\mathrm{ac}\Phi k_0 \sin(2k_0 z)\hat{\boldsymbol{e}}_z\,, \tag{5.19}$$

where $E^\mathrm{ac} = \frac{p_\mathrm{a}^2}{2\rho_0 c_s^2}$ is the acoustic energy-density[6] and $\Phi = \frac{2f_0+3f_1}{12}$ the contrast factor. It is through Φ that f_0 and f_1 determine whether the particles go to a node or an anti-node [3].

The Stokes drag force on a particle is [21]

$$\boldsymbol{F}^\mathrm{drag} = 6\pi\eta_0 b\big(\boldsymbol{U} - \boldsymbol{U}_\mathrm{p}\big) \tag{5.20}$$

where $\boldsymbol{U}$ is the acoustic streaming evaluated at the particle center and $\boldsymbol{U}_\mathrm{p}$ the center-of-mass velocity of the particle.[7] The part of $\boldsymbol{F}^\mathrm{drag}$ which results from the imposed streaming due to the body force (5.5) is denoted by the subscript "imp" for "imposed streaming": $\boldsymbol{F}^\mathrm{drag}_\mathrm{imp}$.

The resultant force on a particle is going to be the sum of Eqs. (5.19) and (5.20), and so the equation of motion for the particle becomes

$$\frac{\mathrm{d}\boldsymbol{P}}{\mathrm{d}t} = \boldsymbol{F}^\mathrm{drag} + \boldsymbol{F}^\mathrm{rad} \tag{5.21}$$

where $\boldsymbol{P} = m\boldsymbol{U}_\mathrm{p}$ is the momentum of the particle and m its mass.

Depending on the sign of Φ, the radiation force $\boldsymbol{F}^\mathrm{rad}$ moves the particle to the node ($\Phi > 0$) or an anti-node ($\Phi < 0$). Simultaneously, the drag force $\boldsymbol{F}^\mathrm{drag}_\mathrm{imp}$ moves the particle in an horizontal direction, and it ultimately arrives and stays in the low temperature region if $\Phi > 0$ and high temperature region if $\Phi < 0$. This is because the imposed streaming in the node goes to the low temperature region and that in the anti-nodes goes to the high temperature region. Hence, particles with different signs on Φ would not only be separated in the vertical direction by the radiation force but also in the horizontal direction by the drag force.

In Fig. 5.9(d)–(e), the resultant force (5.21) on a particle with radius $b = 3\,\mathrm{\mu m}$ is shown for $\Phi > 0$ and $\Phi < 0$, respectively. In (d), we find that the particle is forced via the node to the low temperature region, where—judging from the force vectors—it reaches an equilibrium position. In (e), the particle is instead forced to the high temperature

[6] Since $\rho_0|v_1|^2 \approx \kappa_s|p_1|^2$, the acoustic energy-density (4.1) becomes $E^\mathrm{ac} = 2\frac{\kappa_s|p_1|^2}{4} = \frac{p_\mathrm{e}^2}{2\rho_0 c_s^2}$.

[7] Since $\boldsymbol{U}$ is not asymtotically uniform, it would be more correct to use Faxén's correction [25] which contains an additional term: $\frac{b^2}{6}\nabla^2\boldsymbol{U}$. However, $b \ll h_\mathrm{fl}$ for particles with a radius of a few microns and $\nabla^2 \sim 4/h_\mathrm{fl}^2$, so the correction would be negligible: $b^2/h_\mathrm{fl}^2 \ll 1$.

region via the anti-nodes; but, unlike the case in (d), there is no equilibrium position. The problem in (e) is that the particle not susceptible enough to $\boldsymbol{F}^{\mathrm{rad}}$. This highlights a major flaw with trying to separate particles by a combination of $\boldsymbol{F}^{\mathrm{rad}}$ and $\boldsymbol{F}^{\mathrm{drag}}_{\mathrm{imp}}$: it requires a very specific balance between the two forces, which, in turn, requires a specific set of values of the particle radius b, contrast factor Φ, and imposed streaming magnitude U_0 in the node. While b and Φ are intrinsic to the particles and liquid medium, U_0 may be adjusted per Eq. (5.13) by changing ΔT_0.

The balance that one wants atleast is that $|F^{\mathrm{rad}}| > \frac{2a}{h_{\mathrm{fl}}-2a}|F^{\mathrm{drag}}_{\mathrm{imp}}(z=0)|$ for every particle. This is to ensure that the imposed streaming does not carry the particles away from their desired destination. The streaming can do this when it makes a turn from, e.g., the high temperature region to the low temperature region, as highlighted by the green box in Fig. 5.9(a) and (e). Here $\boldsymbol{F}^{\mathrm{drag}}_{\mathrm{imp}}$ acts almost entirely against $\boldsymbol{F}^{\mathrm{rad}}$. The front-factor $\frac{2a}{h_{\mathrm{fl}}-2a} \approx 0.77$ occurs as a result of mass conservation[8], but one may as well omit it, because this just makes the condition more strict. As $|F^{\mathrm{rad}}| \propto b^3$ and $|F^{\mathrm{drag}}_{\mathrm{imp}}| \propto b$, this becomes very relevant for small particles. Hence, one should evaluate the inquality using the parameters of the smallest particle under consideration.

Another problem arises if $\boldsymbol{F}^{\mathrm{rad}}$ has a horizontal component and the component is greater than $\boldsymbol{F}^{\mathrm{drag}}_{\mathrm{imp}}$. This namely hinders the migration of the particles in the horizontal direction. In Fig. 5.9(e), $\boldsymbol{F}^{\mathrm{rad}}$ has a horizontal component, but $\frac{2a}{h_{\mathrm{fl}}-2a}|F^{\mathrm{drag}}_{\mathrm{imp}}(z=0)| > |F^{\mathrm{rad}}|$, so the particles are not stopped; instead they are carried away with the stream.

Within the realm of particle separation by free-flow acoustophoresis, the length dimension of the channel is reserved for a continuous flow along the length in the x-axis. Since the temperature gradient evidently need to be orthogonal to the radiation force in the z-axis, the temperature gradient is limited to the y-axis in a rectangular channel. This adds another spatial dimension in which to perform the particle separation, but it does not sort particles any differently than existing devices—at best, it improves the succes rate at particle separation at the cost of a more complex device. Finally, it could be interesting to consider alternative channel geometries like a cylindrical one and, in this geometry, investigate the effects of applying the temperature gradient at an angle to the radiation force.

[8]This was discussed in Section 5.2.

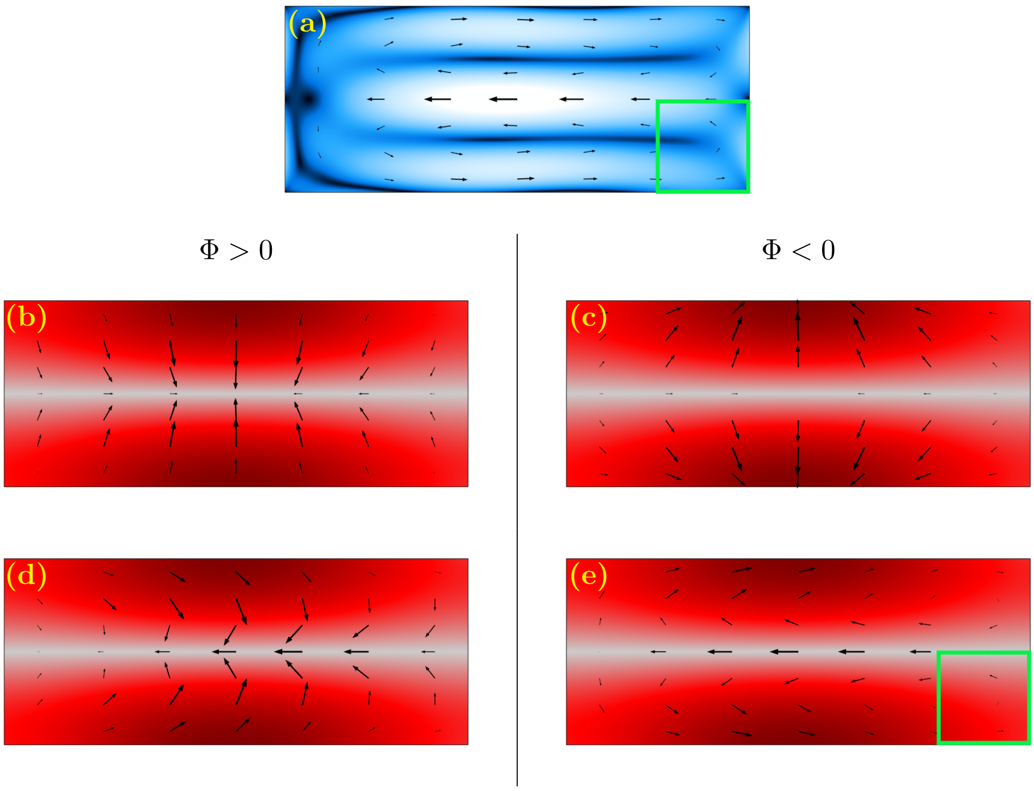

Figure 5.9: (a) The acoustic streaming (surface plot) for the (1,0) eigenmode with $\Delta T_0 = 7\,\mathrm{K}$ and the drag force (arrows) from the acoustic streaming. (b)–(c) The radiation force (arrows) and the pressure magnitude (surface plot) for $\Phi > 0$ and $\Phi < 0$, respectively. (d)–(e) The resultant force (5.21) (arrows) and pressure magnitude (surface plot) for $\Phi > 0$ and $\Phi < 0$, respectively. Particle had a radius of $b = 3\,\mu\mathrm{m}$. Scattering coefficients were $f_0 = -0.075$ and $f_1 = 0.25$ in (d) and $f_0 = -0.135$ and $f_1 = 0.05$ in (e).

Chapter 6

Conclusion and outlook

The effects of an imposed temperature gradient on the acoustic streaming for several acoustic eigenmodes in a water-filled microchannel have been studied in this thesis. The temperature gradient induced gradients in the density and compressibility of the fluid by which it gave rise to an acoustic body force acting on the bulk of the fluid. The body force pointed in the direction of the high temperature region because both the density and compressibility decrease with increasing temperature. Also, the force was strongest in the acoustic pressure anti-nodes, because the compressibility of water is more temperature sensitive than its density.

For the horizontal eigenmodes (1,0) and (2,0), the streaming was intensified in the high temperature region and weakened in the low temperature region. This was related to a skewing in the first-order fields and thus the acoustic body force driving the small stream rolls inside the boundary layers, which, in turn, drive the characteristic stream rolls in the bulk. The skewing was caused by the speed of sound being different between the high and low temperature regions; although, the exact physical mechanism behind it remains unknown.

For the vertical mode (0,1), the acoustic streaming was forced by the acoustic body force to the high temperature region via the anti-nodes and subsequently back by mass conservation to the low temperature region via the node. The potential of using the acoustic streaming induced by the temperature gradient to separate particles in the horizontal direction according to their contrast factor was discussed in a specific setup. For this setup, the conclusion is that it should be possible for very specific—bordering to ideal—conditions: the radiation force should be confined to the vertical direction only and be greater than drag force on the particles from the temperature gradient induced streaming. Achieving separation in the horizontal direction could improve the succes rate of separating particles of different contrast factors. However, this calls for a new design, which is oriented toward applying a temperature gradient to achieve separation.

Appendix A

Thermodynamic derivatives and sensitivities

Table A.1: Thermodynamic derivatives [10] and temperature sensitives $a_q = \frac{1}{\alpha_p}\frac{\partial \ln q}{\partial T}$ [8] at temperature 25 °C and pressure 0.1013 MPa.

Symbol	Value	Units
Thermodynamic derivatives:		
$\frac{\partial \ln \eta}{\partial T}$	-2.278×10^{-2}	K^{-1}
$\frac{\partial \ln \eta}{\partial \rho}$	-3.472×10^{-4}	$\mathrm{kg}^{-1}\,\mathrm{m}^3$
$\frac{\partial \ln \eta^{\mathrm{b}}}{\partial T}$	2.584×10^{-2}	K^{-1}
$\frac{\partial \ln k^{\mathrm{th}}}{\partial T}$	2.697×10^{-3}	K^{-1}
$\frac{\partial \ln k^{\mathrm{th}}}{\partial T}$	2.074×10^{-3}	$\mathrm{kg}^{-1}\,\mathrm{m}^3$
Temperature sensitivities:		
a_ρ	-1	1
a_η	-89	1
$a_{\eta^{\mathrm{b}}}$	-100	1
$a_{k^{\mathrm{th}}}$	11	1
a_{α_p}	145	1
a_{κ_s}	-10	1

Appendix B

Thermal boundary layer

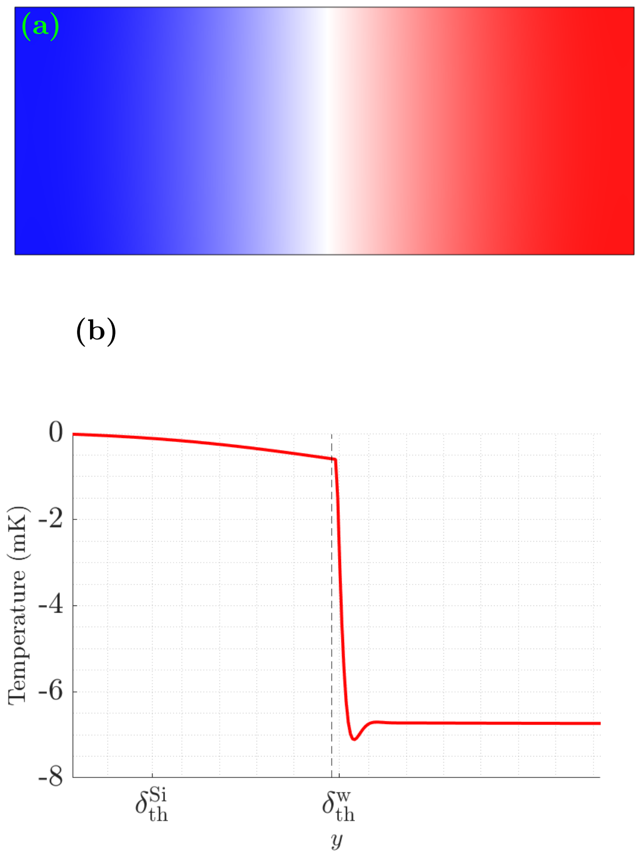

Figure B.1: (a) Temperature field associated with the acoustic wave. (b) Thermal boundary layer in silicon and water in $y = -w_{\text{fl}}/2$. Dashed line indicates the interface between the two materials with silicon on the left and water on the right. Thermal boundary layer thicknesses of the two materials are indicated on the horizontal axis.

Bibliography

[1] P. Delsing, A. Cleland, M. Schuetz, J. Knörzer, G. Giedke, J. Cirac, K. Srinivasan, M. Wu, K. Balram, C. Bäuerle, T. Meunier, C. Ford, P. Santos, E. Cerda-Méndez, H. Wang, H. Krenner, E. Nysten, M. Weiß, G. Nash, L. Thevenard, C. Gourdon, P. Rovillain, M. Marangolo, J.-Y. Duquesne, G. Fischerauer, W. Ruile, A. Reiner, B. Paschke, D. Denysenko, D. Volkmer, A. Wixforth, H. Bruus, M. Wiklund, J. Reboud, J. Cooper, Y. Fu, M. Brugger, F. Rehfeldt, and C. Westerhausen, *The 2019 surface acoustic waves roadmap*. Journal of Physics D: Applied Physics **52**(35) (2019).

[2] M. Wu, A. Ozcelik, J. Rufo, R. Fang, and T. Huang, *Acoustofluidic separation of cells and particles*. Microsystems & Nanoengineering **5** (2019).

[3] A. Lenshof, C. Magnusson, and T. Laurell, *Acoustofluidics 8: Applications of acoustophoresis in continuous flow microsystems*. Lab on a chip **12**, 1210–23 (2012).

[4] M. Evander and J. Nilsson, *Acoustofluidics 20: Applications in acoustic trapping*. Lab on a chip **12**, 4667–76 (2012).

[5] M. Ohlin, A. Christakou, T. Frisk, B. Önfelt, and M. Wiklund, *Influence of acoustic streaming on ultrasonic particle manipulation in a 100-well ring-transducer microplate*. Journal of Micromechanics and Microengineering **23**, 035008 (2013).

[6] P. Li and T. Huang, *Applications of acoustofluidics in bioanalytical chemistry*. Analytical Chemistry **91** (2018).

[7] J. T. Karlsen and H. Bruus, *Forces acting on a small particle in an acoustical field in a thermoviscous fluid*. Phys. Rev. E **92**, 043010 (2015).

[8] J. H. Joergensen and H. Bruus, *Theory of pressure acoustics with thermoviscous boundary layers and streaming in elastic cavities*. The Journal of the Acoustical Society of America **149**(5), 3599–3610 (2021).

[9] W. Qiu, J. H. Joergensen, E. Corato, H. Bruus, and P. Augustsson, *Fast microscale acoustic streaming driven by a temperature-gradient-induced non-dissipative acoustic body force*. `arxiv.org/abs/2103.10192` (2021).

[10] P. B. Muller and H. Bruus, *Numerical study of thermoviscous effects in ultrasound-induced acoustic streaming in microchannels*. Phys. Rev. E **90**, 043016 (2014).

[11] J. Bach and H. Bruus, *Theory of pressure acoustics with viscous boundary layers and streaming in curved elastic cavities.* Acoustical Society of America. Journal **144**(2), 766–784 (2018).

[12] B. Lautrup, *Physics of Continuous Matter: Exotic and Everyday Phenomena in the Macroscopic World* (CRC Press) (2011).

[13] H. Bruus, *Theoretical microfluidics* (Oxford University Press, Oxford) (2007).

[14] H. Bruus, *Numerical studies in physics.* DTU Lecture Notes (2020).

[15] L. Landau and E. Lifshitz, *Fluid Mechanics: Volume 6.* vb. 6 (Elsevier Science, Amsterdam) (2013).

[16] S. Blundell and K. Blundell, *Concepts in Thermal Physics* (Oxford University Press, Oxford) (2010).

[17] L. Landau, L. Pitaevskii, A. Kosevich, and E. Lifshitz, *Theory of Elasticity: Volume 7.* vb. 7 (Elsevier Science, Amsterdam) (2012).

[18] H. Bruus, *Acoustic streaming.* DTU Lecture Notes (2018).

[19] P. B. Muller, R. Barnkob, M. J. H. Jensen, and H. Bruus, *A numerical study of microparticle acoustophoresis driven by acoustic radiation forces and streaming-induced drag forces.* Lab Chip **12**, 4617–4627 (2012).

[20] Private communication (2021), Dr. Wei Qui, Lund University.

[21] N. R. Skov, J. S. Bach, B. G. Winckelmann, and H. Bruus, *3D modeling of acoustofluidics in a liquid-filled cavity including streaming, viscous boundary layers, surrounding solids, and a piezoelectric transducer.* AIMS Mathematics **4**, 99 (2019).

[22] E. Bodenschatz, W. Pesch, and G. Ahlers, *Recent developments in Rayleigh-Bénard convection.* Annual Review of Fluid Mechanics **32**(1), 709–778 (2000).

[23] W. Qiu, J. T. Karlsen, H. Bruus, and P. Augustsson, *Experimental characterization of acoustic streaming in gradients of density and compressibility.* Phys. Rev. Applied **11**, 024018 (2019).

[24] J. T. Karlsen, W. Qiu, P. Augustsson, and H. Bruus, *Acoustic streaming and its suppression in inhomogeneous fluids.* Phys. Rev. Lett. **120**, 054501 (2018).

[25] S. B. Chen and X. Ye, *Faxen's laws of a composite sphere under creeping flow conditions.* Journal of Colloid and Interface Science **221**(1), 50–57 (2000).